Article

Cell Reports

Lethal Poisoning of Cancer Cells by Respiratory Chain Inhibition plus Dimethyl α-Ketoglutarate

Graphical Abstract

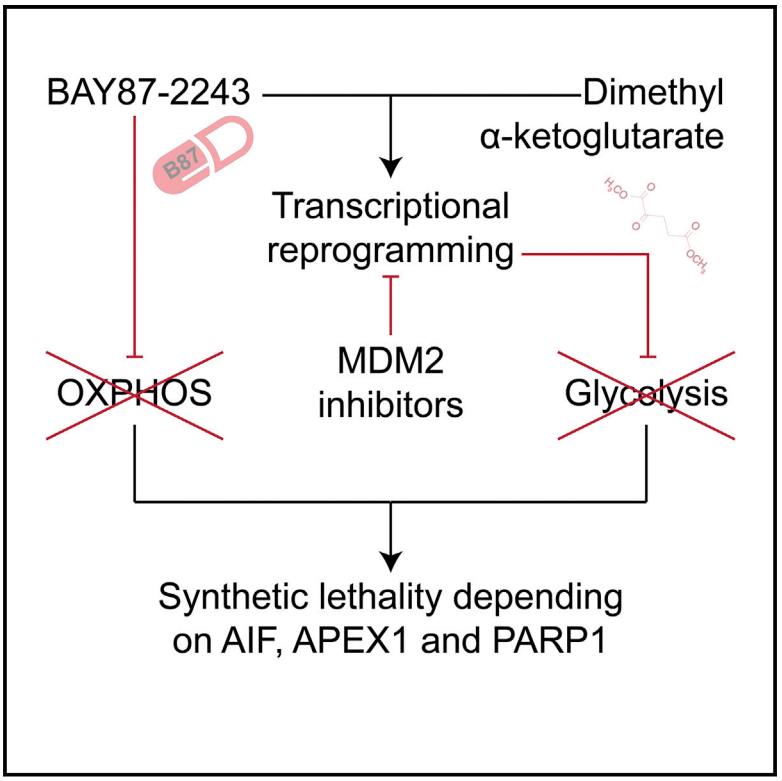

Highlights

- The respiratory chain complex I inhibitor BAY87-2243 (B87) fails to kill cancer cells
- B87 combined with dimethyl alpha-ketoglutarate (DMKG) causes cancer cell death
- The lethal action of B87 + DMKG requires MDM2 but not TP53
- B87 plus DMKG shuts off glycolysis through MDM2-dependent transcriptional reprogramming

Authors

Valentina Sica,
Jose Manuel Bravo-San Pedro,
Valentina Izzo, ..., Karl Ziegelbauer,
Guido Kroemer, Maria Chiara Maiuri

Correspondence

kroemer@orange.fr (G.K.),
chiara.maiuri@upmc.fr (M.C.M.)

In Brief

Sica et al. show that respiratory chain inhibition by 1-cyclopropyl-4-(4-[(5-methyl-3-(3-[4-(trifluoromethoxy)phenyl]-1,2,4-oxadiazol-5-yl)-1H-pyrazol-1-yl)methyl]pyridin-2-yl)piperazine (BAY87-2243, abbreviated as B87) becomes lethal for cancer cells when glycolysis is simultaneously suppressed. When combined with B87, dimethyl α-ketoglutarate acquires the capacity to suppress glycolysis, thus lethally poisoning bioenergetics metabolism. This therapeutic combination effect relies on transcriptional reprogramming that can be reverted by pharmacological inhibition of MDM2.

Sica et al., 2019, Cell Reports *27*, 820–834
April 16, 2019
https://doi.org/10.1016/j.celrep.2019.03.058

CellPress

OPEN ACCESS
CellPress

Cell Reports
Article

Lethal Poisoning of Cancer Cells by Respiratory Chain Inhibition plus Dimethyl α-Ketoglutarate

Valentina Sica,[1,2,13] Jose Manuel Bravo-San Pedro,[1,2,13] Valentina Izzo,[1,2] Jonathan Pol,[1,2] Sandra Pierredon,[3] David Enot,[1,2] Sylvère Durand,[1,2] Noélie Bossut,[1,2] Alexis Chery,[1,2] Sylvie Souquere,[4] Gerard Pierron,[4] Evangelia Vartholomaiou,[3] Naoufal Zamzami,[1,2] Thierry Soussi,[1,2,5] Allan Sauvat,[1,2] Laura Mondragón,[1,2] Oliver Kepp,[1,2] Lorenzo Galluzzi,[1,6,7,8] Jean-Claude Martinou,[3] Holger Hess-Stumpp,[9] Karl Ziegelbauer,[10] Guido Kroemer,[1,2,11,12,14,15,*] and Maria Chiara Maiuri[1,2,14,*]

[1]Centre de Recherche des Cordeliers, INSERM, Sorbonne Université, USPC, Université Paris Descartes, Université Paris Diderot, Equipe 11 labellisée par la Ligue contre le Cancer, 75006 Paris, France
[2]Metabolomics and Cell Biology Platforms, Institut Gustave Roussy, 94805 Villejuif, France
[3]Department of Cell Biology, University of Geneva, 1211 Geneva, Switzerland
[4]CNRS-UMR-9196, Institut Gustave Roussy, 94805 Villejuif, France
[5]Department of Oncology-Pathology, Cancer Center Karolinska (CCK), Karolinska Institutet, 17176 Stockholm, Sweden
[6]Department of Radiation Oncology, Weill Cornell Medical College, New York, NY 10065, USA
[7]Sandra and Edward Meyer Cancer Center, New York, NY 10065, USA
[8]Department of Dermatology, Yale University School of Medicine, New Haven, CT 06510, USA
[9]Global Drug Discovery, Bayer Pharma AG, 13353 Berlin, Germany
[10]Research & Development, Pharmaceuticals, Bayer AG, 42117 Wuppertal, Germany
[11]Pôle de Biologie, Hôpital Européen Georges Pompidou, AP-HP, 75015 Paris, France
[12]Karolinska Institute, Department of Women's and Children's Health, Karolinska University Hospital, 17176 Stockholm, Sweden
[13]These authors contributed equally
[14]Senior author
[15]Lead Contact
*Correspondence: kroemer@orange.fr (G.K.), chiara.maiuri@upmc.fr (M.C.M.)
https://doi.org/10.1016/j.celrep.2019.03.058

SUMMARY

Inhibition of oxidative phosphorylation (OXPHOS) by 1-cyclopropyl-4-(4-[(5-methyl-3-(3-[4-(trifluoromethoxy)phenyl]-1,2,4-oxadiazol-5-yl)-1H-pyrazol-1-yl) methyl]pyridin-2-yl)piperazine (BAY87-2243, abbreviated as B87), a complex I inhibitor, fails to kill human cancer cells *in vitro*. Driven by this consideration, we attempted to identify agents that engage in synthetically lethal interactions with B87. Here, we report that dimethyl α-ketoglutarate (DMKG), a cell-permeable precursor of α-ketoglutarate that lacks toxicity on its own, kills cancer cells when combined with B87 or other inhibitors of OXPHOS. DMKG improved the antineoplastic effect of B87, both *in vitro* and *in vivo*. This combination caused MDM2-dependent, tumor suppressor protein p53 (TP53)-independent transcriptional reprogramming and alternative exon usage affecting multiple glycolytic enzymes, completely blocking glycolysis. Simultaneous inhibition of OXPHOS and glycolysis provoked a bioenergetic catastrophe culminating in the activation of a cell death program that involved disruption of the mitochondrial network and activation of PARP1, AIFM1, and APEX1. These results unveil a metabolic liability of human cancer cells that may be harnessed for the development of therapeutic regimens.

INTRODUCTION

Throughout the past decade, mitochondria have emerged as a promising target for the development of anticancer regimens (Fulda et al., 2010; Green et al., 2014; Wallace, 2012). In particular, the key role of these organelles in the control of multiple signal transduction cascades involved in regulated cell death (RCD) has been harnessed to generate inhibitors of the BCL2 apoptosis regulator (BCL2), which normally prevents mitochondrial membranes from getting permeabilized and releasing pro-apoptotic factors into the cytosol (Green and Reed, 1998; Kroemer and Reed, 2000). One such BCL2 inhibitor, venetoclax, has received regulatory approval for the treatment of subjects with chronic lymphocytic leukemia who have relapsed from, or have been refractory to, prior chemotherapy and exhibit chromosome 17p deletion (Deeks, 2016; Roberts et al., 2016; Souers et al., 2013).

In addition, attempts have been launched to inhibit the vital contribution of mitochondria to cellular metabolism. Indeed, contrary to old beliefs that arose by the misinterpretation of the so-called Warburg effect (the increased use of glucose by normoxic cancer cells), mitochondria mediate critical bioenergetic and anabolic functions not only in normal but also in malignant cells (Fogal et al., 2010; Fulda et al., 2010; Galluzzi et al., 2006;

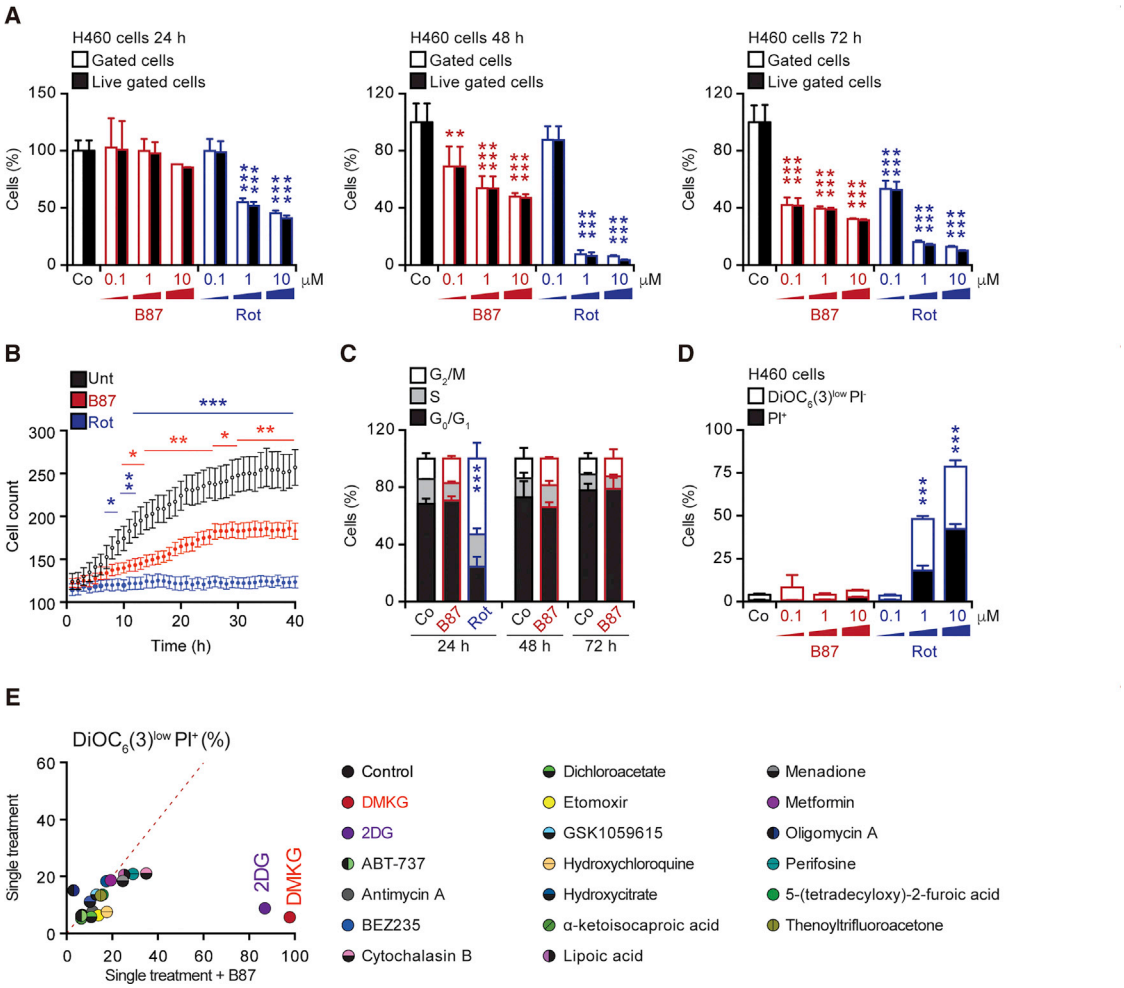

Figure 1. The *Per Se* Limited Cytotoxic Effect of B87 Is Exacerbated by Dimethyl α-Ketoglutarate

(A and B) Evaluation of anti-proliferative effect of B87.

(A) H460 cells were treated as indicated and the absolute cell count (as a percentage) was measured by flow cytometry for the total gated cells and the live-gated cells (meaning that PI^+ cells were excluded). n = 3–6.

(B) Cells were treated and recorded to show the proliferation rate in real time. The graph represents the total cell count over time. n = 9.

(C) Evaluation of B87 effects on cell cycle progression. Student's t test was calculated between the G_2 and M phases of each condition. n = 4.

(D) Cytometric quantification of cell death. H460 cells were treated as indicated and then double stained with PI and $DiOC_6(3)$ for the detection of dying ($DiOC_6(3)^{low}$ PI^-) and dead (PI^+) cells. n = 3–6.

(E) Identification of DMKG as a synthetic lethal interactor with complex I inhibition. Cells were treated with B87 in the presence or absence (single treatment) of each of the 19 compounds listed, followed by the cytofluorimetric detection of cell death. n = 3–4.

Columns indicate means ± SD. Symbols indicate significant (unpaired Student's t test or Sidak's multiple comparisons test, E); see also Table S2) changes with respect to controls (*p < 0.05, **p < 0.01, ***p < 0.001). The figures are representative of three independent experiments yielding similar results.

Drugs concentration and time of treatments are detailed in Tables S2 and S6.

Green et al., 2014; Maddocks et al., 2017; Roberts et al., 2016; Weinberg et al., 2010; Wheaton et al., 2014). In this context, the antineoplastic effects of various agents have been (at least partially) attributed to their ability to target mitochondria in malignant (but not normal) cells (Galluzzi et al., 2013). As a stand-alone example, metformin (a biguanide commonly employed for the treatment of type II diabetes) was proven to mediate anticancer effects also by means of its capacity to inhibit respiratory complex I (Wheaton et al., 2014). However, as metformin must be used at millimolar concentrations to achieve complex I inhibition *in vitro*, doubts have been raised on its actual mechanism of action *in vivo*. A recently developed highly specific complex I inhibitor, 1-cyclopropyl-4-(4-[(5-methyl-3-(3-[4-(trifluoromethoxy) phenyl]-1,2,4-oxadiazol-5-yl)-1H-pyrazol-1-yl)methyl]pyridin-2-yl)piperazine (BAY87-2243, abbreviated as B87), inhibited the proliferation of human cancer cells, including melanoma cells, *in vitro* (Ellinghaus et al., 2013) and *in vivo* (Schöckel et al., 2015). Moreover, B87 efficiently improved local tumor control by fractionated irradiation in a xenograft model of head and neck cancer (Helbig et al., 2014). In contrast to the widely used experimental complex I inhibitor rotenone (Srivastava and Panda, 2007), B87 does not alter microtubular polymerization

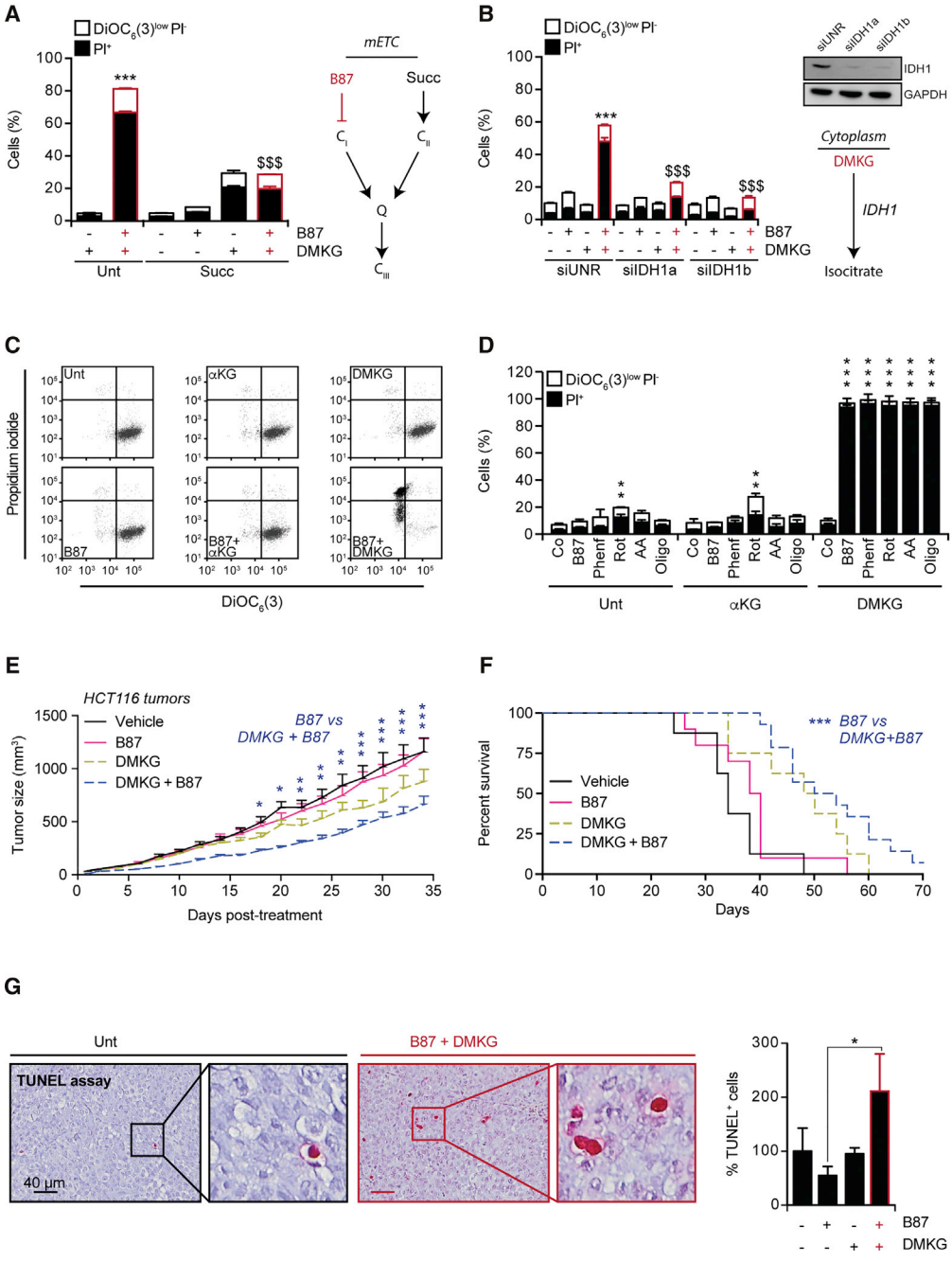

Figure 2. Cancer Cells Succumb to Respiratory Chain Complexes Inhibitors in the Presence of Dimethyl α-Ketoglutarate

(A) Succinate (Succ)-mediated rescue from the lethal effect of B87 plus DMKG. H460 cells were treated as indicated and followed by double staining with PI and $DiOC_6(3)$ for the detection of dying ($DiOC_6(3)^{low}$ PI^-) and dead (PI^+) cells. n = 3.

(B) Contribution of isocitrate dehydrogenase (IDH1) to cell killing by B87 plus DMKG. H460 cells were transfected with unrelated (UNR) siRNA or two distinct siRNAs targeting IDH1 for 48 h and treated as indicated. After the treatments, cells were collected and cell death was analyzed by cytofluorimetry. n = 3.

(C and D) Synthetic lethal interaction between DMKG and mitochondrial respiratory chain inhibitors. H460 cells were treated as indicated and cell death was analyzed by cytofluorimetry. Representative flow cytometry plots (C) and quantification of cell death upon PI and $DiOC_6(3)$ staining (D) are shown. n = 3.

Columns indicate means ± SD. Symbols indicate significant (unpaired Student's t test) changes with respect to controls (**$p < 0.01$ and ***$p < 0.001$) or to B87 plus DMKG ($^{\$\$\$}p < 0.001$). The figures are representative of three independent experiments yielding similar results.

(E and F) *In vivo* antitumor effects of DMKG combined with B87. Immunodeficient mice bearing palpable subcutaneous HCT116 derived cancers were treated with B87 alone or in combination with DMKG. Tumors volume (E) was estimated in mice treated as indicated. Kaplan-Meier of the overall survival (F). n ≥ 8.

(G) Representative TUNEL-stained images and quantification of tumors slides. n ≥ 3.

(legend continued on next page)

rates, hence lacking antimitotic (and hence toxic) activity. Notably, introduction of yeast nicotinamide adenine dinucleotide (NADH)-Q-oxidoreductase into human cells abrogated the antiproliferative activity of B87, clearly demonstrating that this molecule operates via an exquisite on-target effect, namely, by inhibiting the NADH oxidase activity of respiratory complex I (Ellinghaus et al., 2013).

That said, effective anticancer treatments that selectively target oxidative phosphorylation (OXPHOS) and mitochondrial metabolism have not yet reached clinical development, at least in part because of specificity issues. Indeed, targeting OXPHOS or other mitochondrial functions with systemic interventions may harm normal tissues with an elevated energy demand, in particular the central nervous system (Lapointe et al., 2004). To circumvent this issue, local administration routes that mostly spare systemic circulation have been devised (Wolinsky et al., 2012). In addition, attention has been attracted by the possibility of using combinatorial regimens based on two anticancer agents with virtually independent mechanisms of action employed at suboptimal doses (Torrance et al., 2000).

Driven by these considerations, we performed a systematic screen to identify agents that might cause synthetic lethality if combined with B87 or other OXPHOS inhibitors. Here, we report that dimethyl α-ketoglutarate (DMKG), can mediate such a synthetically lethal effect, both *in vitro* and *in vivo*. Our findings unravel a complex lethal signaling pathway that involves MDM2-dependent transcriptional reprogramming culminating with glycolytic inhibition, followed by the activation of an atypical cell death program.

RESULTS

The Complex I Inhibitor B87 Fails to Kill Human Cancer Cells

Two human adenocarcinoma cell lines, namely H460 (non-small cell lung carcinoma) and HCT116 (colorectal carcinoma) were retarded in their proliferation by B87, a highly selective complex I inhibitor, as determined by cell counting by cytofluorimetric analysis (Figures 1A and S1A), or by using bright field microscopy recording (Figure 1B) or analysis of cell division by dilution of carboxyfluorescein succinimidyl ester (CFSE) (Figure S1B). However, the effect of B87 was less pronounced than that observed with rotenone (Figures 1A and 1B), which is known to inhibit complex I as well as interfering with microtubule assembly (Srivastava and Panda, 2007). Accordingly, rotenone, but not B87, caused an accumulation of cells in the G_2/M phases of the cell cycle (Figures 1C and S1C). B87 reduced cell proliferation without causing an arrest in a specific phase of the cell cycle but slowed down the cell division rate. However, H460 and HCT116 cells exposed to B87 up to 72 h failed to exhibit signs of cell death (Figures 1D and S1D), including the uptake of the vital dye propidium iodide (PI) and the dissipation of mitochondrial transmembrane potential as assessed by 3,3-dihexyloxacarbocyanine iodide ($DiOC_6(3)$) staining. Conversely, rotenone killed a sizable fraction of the H460 (Figure 1D) and HCT116 cells (Figure S1D). Altogether, these results suggest that B87 has no major cytotoxic activity while it retards cell division.

Cancer Cells Succumb to Complex I Inhibition in the Presence of Dimethyl α-Ketoglutarate

We screened a library comprising 67 experimental and approved cytostatic or cytotoxic anticancer agents for potential synergistic interactions with B87. However, none among the tested agents exhibited increased cytotoxic activity in the presence of B87 (Figure S1E; Table S1). Among a series of distinct metabolic modulators, we observed no synergistic interactions with B87 for the BCL2 inhibitor ABT-737; the respiratory chain inhibitors metformin, antimycin A, thenoyltrifluoroacetone, and oligomycin A; the inhibitor of new actin filament assembly, cytochalasin B; the redox cycling agent, menadione; the AKT/PI3K/mTOR inhibitors, perifosine, GSK1059615, and BEZ235; the ATP citrate lyase inhibitor, hydroxycitrate; the acetyl-CoA carboxylase inhibitor, 5-(tetradecyloxy)-2-furoic acid; the irreversible inhibitor of carnitine palmitoyltransferase-1, etomoxir; the inhibitor of pyruvate dehydrogenase kinase 1, dichloroacetate; and the autophagy inhibitors, α-ketoisocaproic acid, hydroxychloroquine, and lipoic acid (Mariño et al., 2014). However, 2-deoxyglucose (2DG), a glucose analog that inhibits glycolysis, mediated synthetic lethality when combined with B87. We observed that DMKG also killed H460 cells when combined with B87 or rotenone (Figures 1E and S1F; Table S2).

The cytotoxicity induced by the combination of B87 and DMKG could be reduced by addition of cell-permeable succinate (dimethyl succinate), a mitochondrial electron transport chain complex II substrate (Figure 2A), as well as by knocking down isocitrate dehydrogenase-1 (IDH1) with two distinct small-interfering RNAs (siRNAs) (Figure 2B). These results confirm that inhibition of the respiratory chain (bypassed by succinate) coupled to the metabolic activity of DMKG, which may require (reverse) conversion by IDH1 to isocitrate in the cytosol, accounts for the synergistic cytotoxicity of B87 plus DMKG.

Accordingly, DMKG (but not αKG, which is not cell permeable) killed cancer cells when combined with a panel of distinct, chemically unrelated complex I inhibitors (B87, rotenone, or phenformin) or other respiratory chain inhibitors (i.e., antimycin A, which targets complex III, or oligomycin A, which inhibits the F_OF_1 ATP synthase activity of complex V) (Figures 2C and 2D). Chessboard representation of flow cytometry detection of the cell count (Figure S2A) and cell death (Figure S2B) confirmed that B87 plus DMKG mediates synergistic lethality. Interestingly, while B87 plus DMKG efficiently killed breast cancer MCF7 cells (Figure S2C), human colon adenocarcinoma HT-29 cells (Figure S2D), neuroglioma H4 cells (Figure S2E), osteosarcoma U-2 OS cells (Figure S2F) as well as H460 and HCT116, it did not affect non-transformed breast epithelial MCF10A cells

Columns indicate means ± SEM Statistical analysis was performed by two-way analysis of variance (ANOVA) followed by Sidak's multiple comparisons test (E), log rank (Mantel-Cox) test (F), and unpaired Student's t test (G). *$p < 0.05$, **$p < 0.01$, and ***$p < 0.001$ (B87 versus B87 plus DMKG). αKG, alpha-ketoglutarate; AA, antimycin A; mETC, mitochondrial electron transport chain; Oligo, oligomycin A; Phenf, phenformin; Rot, rotenone.
Drug concentrations and times of treatments are detailed in Table S6.

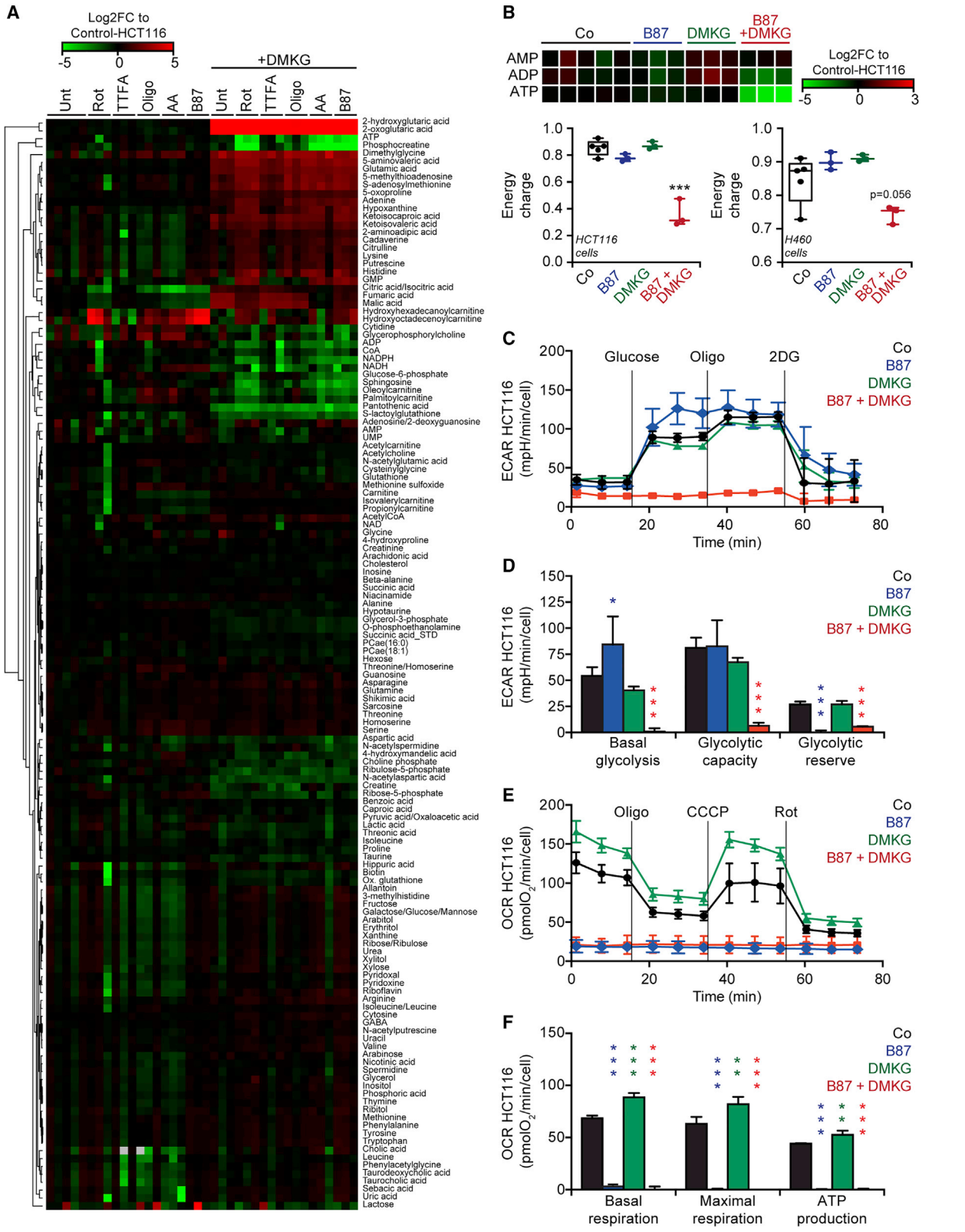

(legend on next page)

(Figure S2G), lung bronchial epithelial 16HBE cells (Figure S2H), and primary human adipocytes (Figure S2I).

Importantly, DMKG failed to limit the growth of H460 or HCT116 tumors established in immunodeficient mice when administered alone, yet significantly enhanced the antineoplastic effects of B87 (Figures 2E and S2J). The combination of B87 plus DMKG was particularly efficient in prolonging the survival of tumor-bearing mice (Figure 2F) while inducing TUNEL positivity in a small, though significant fraction of cancer cells (Figure 2G). Altogether, these results reveal the synergistic potential of B87 plus DMKG against human cancer cells.

Bioenergetic Catastrophe Induced by Combination Treatment with B87 and DMKG

We profiled the intracellular metabolome of HCT116 and H460 cells treated with respiratory chain inhibitors (B87, rotenone, 5-(tetradecyloxy)-2-furoic acid [TTFA], oligomycin A, and antimycin A) alone or in combination with DMKG at 6 h, a time point when >70% of the cells were still viable (Figures 3A and S3A; Table S3). In line with the role of DMKG as an anaplerotic substrate, DMKG increased the abundance of several tricarboxylic acid (TCA) cycle intermediates irrespective of the absence or presence of respiratory chain inhibitors. However, the combination of respiratory chain inhibitors and DMKG (but none of them used alone) caused a drastic depletion in intracellular ATP and energy charge (Figures 3B and S3B). The extracellular acidification rate (ECAR), a proxy of glycolysis, in HCT116 and H460 cells was strongly inhibited in the presence of B87 plus DMKG (Figures 3C, 3D, and S3C) (but not by either of the two agents alone). Notably, stand-alone DMKG did not inhibit mitochondrial respiration and rather enhanced O_2 consumption in HCT116 and H460 cells, an effect that was completely abrogated by B87 (Figures 3E, 3F, and S3D).

Attempts to avoid cell killing by B87 plus DMKG using cell permeable pyruvate (methyl pyruvate) (Figure S3E), as well as excess glucose, pyruvate, or glutamine (alone or in combination), failed (Figure S3F). Altogether, these results indicate that inhibition of the respiratory chain plus DMKG strongly suppresses glycolysis, hence precipitating a lethal bioenergetic crisis.

DMKG plus B87 Kills Cancer Cells through MDM2-Dependent Parthanatos

Transmission electron microscopy failed to reveal signs of apoptosis such as chromatin condensation and nuclear fragmentation in H460 cells exposed to B87 plus DMKG, yet revealed mitochondrial swelling with a rarefaction of cristae (Figure 4A). Immunofluorescence microscopy followed by morphometric analyses confirmed that B87 plus DMKG (but neither of the two agents alone) increased the granularity of mitochondria, identified as $TOMM20^+$ objects (Figures 4B and 4C), reflecting fragmentation of the mitochondrial network, and augmented the mean mitochondrial diameter (Figures 4B and 4D). B87 plus DMKG killed HCT116 cells lacking the pro-apoptotic multidomain BCL2 family proteins BAX and BAK as effectively as wild-type (WT) cells, although the $BAX^{-/-}BAK1^{-/-}$ genotype conferred complete protection against the lethal effect of the tyrosine kinase inhibitor staurosporine. Moreover, tumor suppressor protein p53 (TP53) was dispensable for cell killing by B87 plus DMKG (Figure 4E).

In an attempt to clarify the cell death pathway activated by B87 plus DMKG, we added several agents known to interfere with apoptosis (Z-VAD-fmk), necroptosis (necrostatin-1), oxidative stress (glutathione ethyl ester; *N*-acetyl cysteine), ferroptosis (ferrostatin-1), TP53 activation (cyclic pifithrin-α), and parthanatos (CEP1, PJ-34, and diphenylene iodonium [DPI]). Among these agents, only the inhibitors of poly(ADP-ribose) polymerase 1 (PARP1): CEP1 and PJ-34, and the inhibitor of apoptosis inducing factor mitochondria associated 1 (AIFM1; best known as AIF) DPI, could reduce killing by B87 plus DMKG, supporting the idea that cancer cells died for parthanatos (Andrabi et al., 2008). The inhibitor of the 26S proteasome MG132, which acts downstream of MDM2 (Fu et al., 2009; Kisselev and Goldberg, 2001), and two agents that are supposed to act on the physical and/or functional MDM2-TP53 interaction, RITA and Nutlin3 (Bálint et al., 1999; Chen et al., 2003; Juven-Gershon et al., 1998; Martin et al., 1995; Shen and Maki, 2011), fully abolished the cytotoxic activity of the B87 and DMKG (Figure 4F; Table S4) and abrogated its ability to disrupt mitochondrial morphology (Figures S4A–S4C).

To confirm the pharmacological results, knockdown of *MDM2* with specific siRNAs reduced cell killing by B87 plus DMKG (Figures 5A and S5A). Similar cytoprotective effects were obtained upon knockdown of *PARP1* (Figures 5B and S5B) and knockout of *AIFM1* (Figures 5C and S5C). Moreover, both the depletion (by specific siRNAs) (Figures 5D and S5D) and the pharmacological inhibition (by E3330) (Figure 5E) of apurinic-apyrimidinic endodeoxyribonuclease 1 (APEX1), an endonuclease known to interact with MDM2 (Busso et al., 2009), counteracted the lethal effect of B87 plus DMKG. APEX1 was upregulated upon treatment with B87 plus DMKG, and this effect was blocked by RITA and Nutlin3 (Figure S5H), suggesting that APEX1 operates downstream of MDM2. To be active, APEX1 must be deacetylated by sirtuin 1 (SIRT1) (Antoniali et al., 2014; Yamamori et al., 2010). Accordingly, depletion (by specific siRNAs) (Figures 5F and S5E) or pharmacological inhibition (by EX527 or nicotinamide, NAM) (Figures 5G and 5H) of this deacetylase prevented the cytotoxic activity of B87 plus DMKG. However, the knockout

Figure 3. Bioenergetic Catastrophe Induced by Combination Treatment with B87 and Dimethyl α-Ketoglutarate

(A and B) Mass spectrometric metabolomic profile of cells treated as indicated for 6 h. Metabolites analyzed are arranged in heatmaps, as indicated by the color scales (A). Energy charge was calculated using the formula: EC = ATP + 1/2ADP/ATP + ADP + AMP (B). n = 3–5.

(C–F) Effects of B87 and DMKG on glycolysis and oxygen consumption. HCT116 cells were analyzed by a Seahorse apparatus to measure glycolysis by means of the extracellular acidification rate (ECAR) (C and D) and oxygen consumption measurements (OCR) (E and F). n = 5.

Columns indicate means ± SD. Symbols indicate significant (unpaired Student's t test) changes with respect to untreated controls (*$p < 0.05$, **$p < 0.01$, and ***$p < 0.001$). The figures are representative of three independent experiments yielding similar results.

Drug concentrations and times of treatments are detailed in Tables S3 and S6.

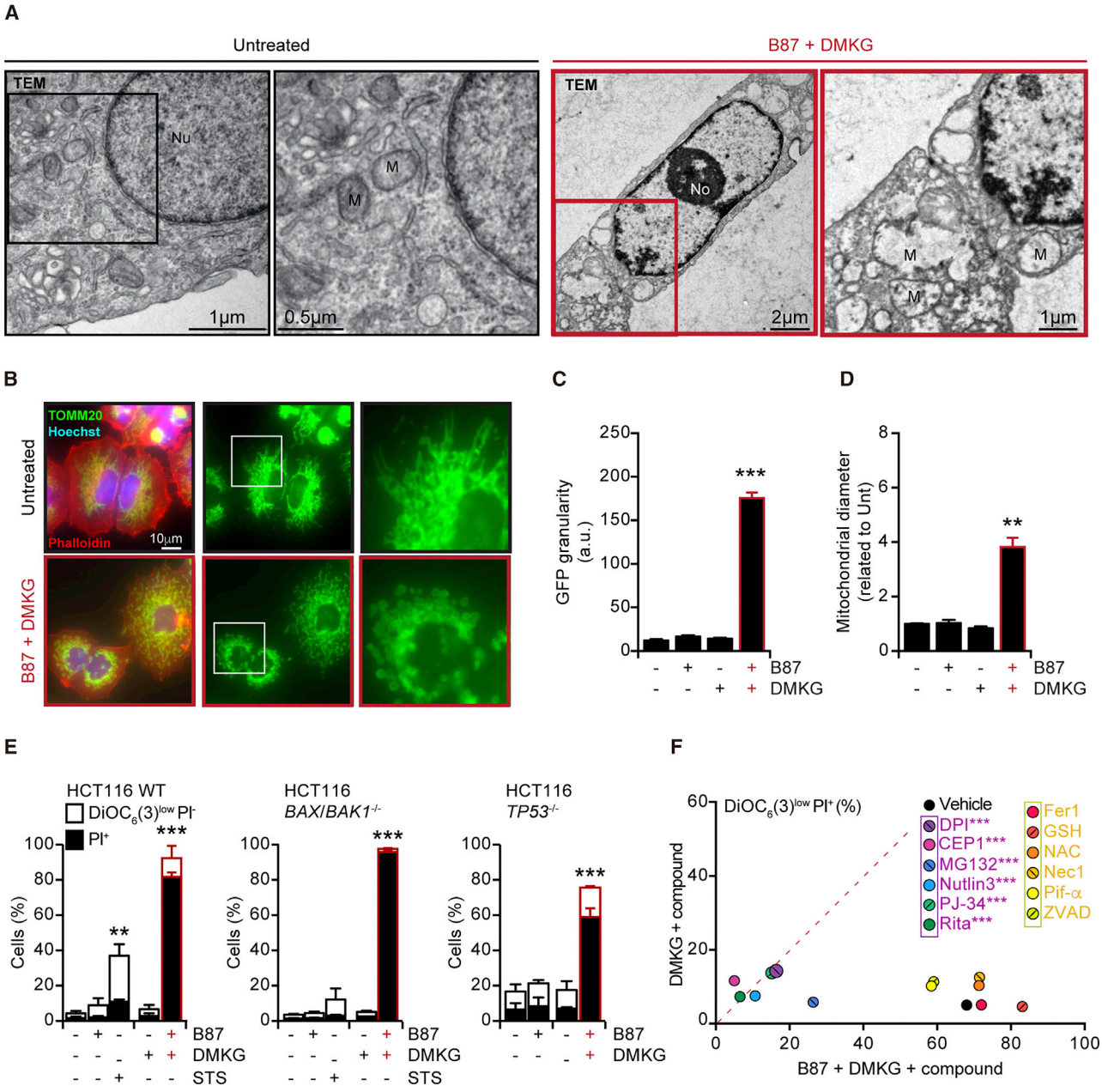

Figure 4. The Combination of B87 and Dimethyl α-Ketoglutarate Kills Cancer Cells through an MDM2-Dependent Mechanism

(A) Ultrastructural analysis of cells. H460 cells were treated and analyzed by transmission electron microscopy to assess mitochondrial (M), nucleus (Nu), and nucleolus (No) morphology.

(B–D) Quantitative analysis of mitochondrial morphology.

(B) Representative images of TOMM20 (green) plus phalloidin (red) immunofluorescence and Hoechst 33342 (blue) staining of H460 cells treated as indicated.

(C and D) Quantification of mitochondrial granularity (C) and diameter (D) is shown. n = 3. a.u., arbitrary units.

(E) Contribution of BAX, BAK, and TP53 to cell death observed after B87 plus DMKG treatment. HCT116 cells WT and their *BAX*$^{-/-}$, *BAK*$^{-/-}$, or *TP53*$^{-/-}$ counterparts were treated and double stained with PI and $DiOC_6(3)$ for the detection of dying ($DiOC_6(3)^{low}$ PI^-) and dead (PI^+) cells. Staurosporine (STS) was used as a positive control of apoptosis induction. n = 3–4.

(F) Identification of inhibitors of cell killing by B87 plus DMKG. H460 cells were treated with DMKG alone or together with B87 in the presence or absence of the following compounds: Nutlin3, RITA, diphenylene iodonium (DPI), the PARP1 inhibitors PJ-34 and CEP1, MG132, necrostatin-1 (Nec1), the caspase inhibitors Z-VAD-fmk (ZVAD), reduced glutathione (GSH), N-acetyl cysteine (NAC), and ferrostatin-1 (Fer1) or pifithrin-α (Pif-α), followed by double staining with PI and $DiOC_6(3)$ for the detection of dead (PI^+) cells. n = 3.

Columns indicate means ± SD. Symbols indicate significant (unpaired Student's t test) changes with respect to controls (**$p < 0.01$ and ***$p < 0.001$). The figures are representative of three independent experiments yielding similar results.

Drugs concentration and time of treatments are detailed in Tables S4 and S6.

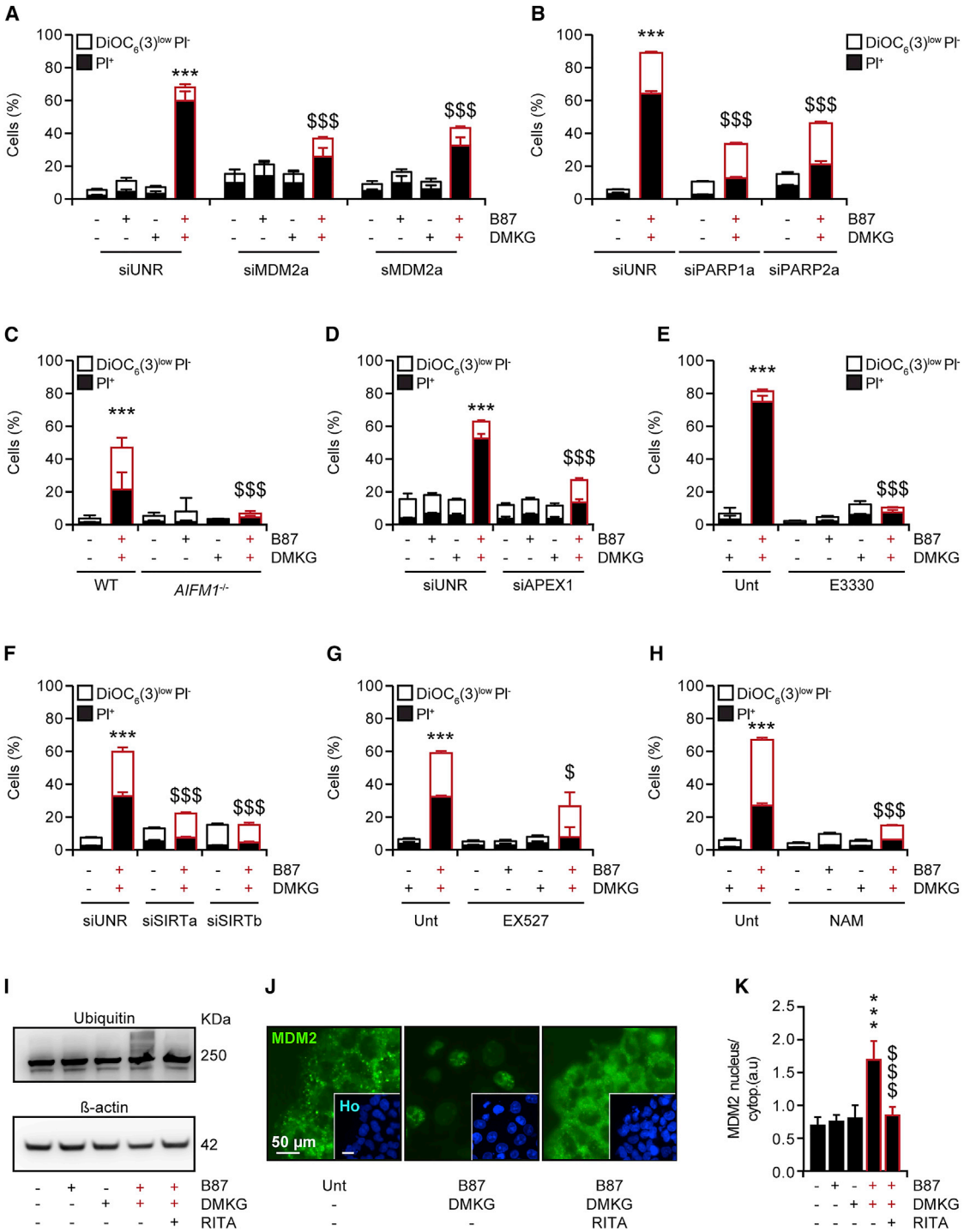

Figure 5. The Combination of B87 and Dimethyl α-Ketoglutarate Kills Cancer Cells through MDM2-Dependent Parthanatos

(A–H) Cytometric quantification of cell death rescuing by using unrelated siRNA (siUNR) or two non-overlapping siRNAs for gene silencing of MDM2 (A), PARP1 (B), APEX1 (D), or SIRT (F); deletion of *AIFM1* (C); chemical inhibition of APEX1 (E); or chemical inhibition of SIRT1 by EX527 (G) and nicotinamide (NAM) (H). H460 cells were treated, collected, and double stained with PI and $DiOC_6(3)$ for the detection of dying ($DiOC_6(3)^{low}$ PI^-) and dead (PI^+) cells. $n \geq 3$.

(I) The presence of ubiquitinated residues upon the indicated treatments, in H460 cells, was assessed by western blot. Antibody for β-actin was employed as a loading control.

(legend continued on next page)

of TP53 (Bunz et al., 1999) or its knockdown with two distinct non-overlapping siRNAs (Figures S5F and S5G) failed to affect cell killing by B87 plus DMKG, as well as its rescue by Nutlin3 or RITA (Figures S5I and S5J), suggesting that MDM2 must act on substrates other than TP53 to induce cell death in this setting (Mikawa et al., 2014; Way et al., 2016). Indeed, RITA and Nutlin3 prevented the degradation of FOXO1 and HSP70 that was induced by B87 plus DMKG, exemplifying that these agents act on other MDM2 substrates (Figure S5K). Moreover, RITA and Nutlin3 inhibited the upregulation of the total cellular levels of AIFM1, APEX1, IDH1, and SIRT1 in response to B87 plus DMKG (Figure S5H). An increased level of ubiquitination of cellular proteins that could be inhibited by RITA (Figure 5I) was found upon B87 plus DMKG treatment. Moreover, the dual treatment induced the translocation of MDM2 to the nucleus (but not mitochondria) that was suppressed by RITA (Figures 5J, 5K, and S5L). Confirming our previous results, the nuclear translocation of MDM2 was not depending on TP53 (Figure S5M).

Altogether, these results indicate that the combination of DMKG and B87 kills susceptible cancer cells through an atypical cell death pathway that involves nuclear (but not mitochondrial) translocation of MDM2, as well as AIFM1, APEX1, PARP1, and SIRT1.

MDM2 Inhibitors Reverse the Transcriptional Effects of DMKG plus B87

The lethal effect of DMKG plus B87 was lost when gene transcription or mRNA translation was blocked with actinomycin D (ActD) or cycloheximide (CHX) (Figure 6A). RNA-sequencing studies (Figure 6B) revealed that DMKG plus B87 induced a unique alteration in gene expression, with the TP53 (Figure 6C) signaling pathway being negatively affected, coherently with its degradation (Figure S6A). Indeed, the expression of several TP53 target genes including phorbol-12-myristate-13-acetate-induced protein 1 (*PMAIP1*), siah E3 ubiquitin protein ligase 1 (*SIAH1*), cyclin G1 (*CCNG1*), and sestrins 1 and 2 (*SESN1* and *SESN2*) in H460 cells concomitantly exposed to DMKG plus B87 was considerably reduced (Figures 6B and 6C). These genes were re-expressed in the presence of RITA or Nutlin3 (Figure 6B). In line with this analysis, TP53 was lost after treatment with B87 plus DMKG (but not with either agent alone), and this effect was reversed by either Nutlin3 or RITA (Figure S6A). Along similar lines, autophagic flux was inhibited by the combination of B87 and DMKG, but was restored in the presence of MDM2 inhibitors (Figures S6A and S6B), reflecting the role of SESN1 and SESN2 as pro-autophagic factors (Lee et al., 2013; Liang et al., 2016) (Figure 6C). B87 and DMKG caused a strong (> 5-fold) activation of transcription factors and subunits thereof including early growth response 1 (EGR1), AP-1 Jun proto-oncogene, AP-1 transcription factor subunit (JUN), Fos proto-oncogene, AP-1 transcription factor subunit (FOS), FosB proto-oncogene, AP-1 transcription factor subunit (FOSB), and MLX interacting protein like (MLXIPL) (Figure S6C). This latter effect was observed even in the presence of RITA or Nutlin3, suggesting that it does not play a major role in lethal signaling induced by B87 plus DMKG. Beyond quantitative changes in the abundance of mRNAs, the simultaneous administration of B87 and DMKG to H460 cells caused a major alteration in RNA splicing, mostly leading to alternative first and terminal exons, as well as to intron retention (Figure 6D). MDM2 inhibitors again were able to eliminate the negative impact of the B87 plus DMKG combination on RNA splicing (Figure 6D). KEGG analysis pointed to the enrichment of multiple glycolysis-relevant genes (i.e., *ALDH7A1*, *PFKL*, *ADPGK*, *PDHA1*, *GAPDH*, *ALDH3B1*, *ALDH3A1*, *ENO1*, and *HK1*) in this category (Figure 6E).

RITA and Nutlin3 Rescue the Glycolytic Defect Induced by DMKG plus B87

Driven by the aforementioned transcriptomic studies, we investigated the impact of MDM2 inhibition on the bioenergetic catastrophe triggered by B87 plus DMKG. Nutlin3 or RITA avoided ATP depletion induced by B87 plus DMKG in H460 cells (Figure 7A). However, neither of these MDM2 inhibitors reversed the inhibition of oxidative phosphorylation by B87 alone or combined with DMKG (Figures S7A and S7B). To assess the use of pyruvate for energy metabolism, we monitored the activity of a mitochondrial pyruvate carrier (MPC) by means of the so-called RESPYR (for reporter Sensitive to pyruvate) biosensor. When pyruvate was added to H460 cells expressing RESPYR, the fluorescent signal rapidly increased; however, this result was blunted by pre-treatment with B87 plus DMKG (but neither of the two compounds alone), suggesting inhibition of pyruvate transport from the cytosol to the mitochondrial matrix. Notably, RITA could reverse such an inhibitory effect (Figures 7B and 7C). In a subsequent series of experiments, we directly measured the capacity of Nutlin3 and RITA to reinstate glycolytic flux. Nutlin3 and RITA restored baseline glycolysis to normal levels in the HCT116 (Figures 7D and 7E) and H460 cells (Figures S7C and S7D) treated with B87 plus DMKG. Fluxomic analyses based on the mass spectrometric detection of ^{13}C-glucose-derived metabolites confirmed that glucose-6-P (first intermediate of glycolysis) is less abundant in HCT116 and H460 cells treated with B87 plus DMKG (but neither of the two compounds alone), contrasting with a normal ^{13}C-glucose uptake (Figure 7F). Both Nutlin3 and RITA prevented the inhibition of glycolytic flux by B87 plus DMKG. Importantly, the rescue effect of MDM2 inhibitors (or inhibitors of AIFM1, APEX1, SIRT1, and PARP1) on cell death induced by B87 plus DMKG was lost when glycolysis was directly inhibited by 2DG (Figures 7G and 7H; Table S5). When H460 cells were continuously cultured in raising concentrations of B87 plus DMKG for 3 months, they developed resistance against the lethal and antiproliferative effects of the drug combination. Such B87 and DMKG-resistant cells continued to arrest oxygen

(J and K) Representative images of MDM2 (green) immunofluorescence and Hoechst 33342 (Ho, blue) for nuclear staining of H460 cells overpressing a plasmid coding for MDM2 (J). Quantification of MDM2 nuclear translocation is shown (K). n = *14*.

Columns indicate means ± SD. Symbols indicate significant (unpaired Student's t test) changes with respect to untreated controls (***$p < 0.001$), or to B87 plus DMKG ($^{\$}p < 0.05$, $^{\$\$\$}p < 0.001$). The figures are representative of three independent experiments yielding similar results.

Drug concentrations and times of treatments are detailed in Table S6.

A

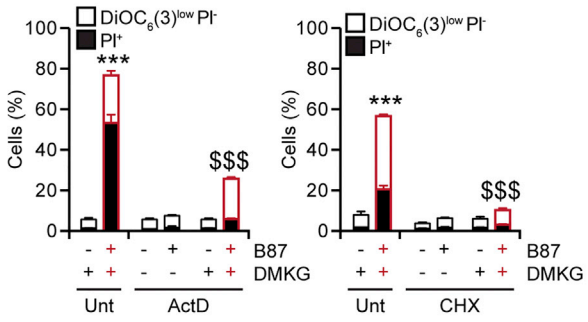

B

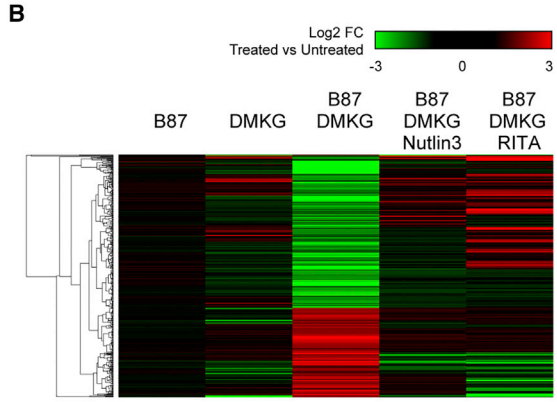

C

Pathway Description (KEGG)	Nb Genes in Pathway	Regulated Genes (Up / Down)	Gene Symbol	Fold-Change	P-Value
p53 signaling pathway (hsa04115)	67	5 (0/5)	PMAIP1	2.89	3.14E-24
			SIAH1	3.07	7.58E-39
			SESN1	2.72	4.72E-22
			CCNG1	2.82	2.00E-25
			SESN2	4.50	1.65E-30
Tuberculosis (hsa05152)	177	7 (1/6)	KSR1	2.70	1.21E-21
			IL1A	5.33	3.21E-24
			CD14	2.92	2.97E-09
			IL1B	3.69	2.14E-07
			CEBPB	2.49	9.24E-10
			CEBPG	2.25	2.46E-24
			C3	2.27	7.66E-12
Amoebiasis (hsa05146)	106	6 (3/3)	COL27A1	3.89	1.74E-29
			IFI30 // PIK3R2	2.00	1.12E-09
			LAMA3	2.82	1.15E-23
			PLCB4	2.49	1.32E-11
			IL1B	3.69	2.14E-07
			CD14	2.92	2.97E-09
Pertussis (hsa05133)	75	4 (0/4)	C3	2.27	7.66E-12
			CD14	2.92	2.97E-09
			IL1B	3.69	2.14E-07
			IL1A	5.33	3.21E-24
Insulin resistance (hsa04931)	108	6 (3/3)	PPP1R3E	2.19	3.41E-05
			PCK2	2.03	3.40E-14
			CREB5	2.59	1.24E-08
			IFI30 // PIK3R2	2.00	1.12E-09
			TRIB3	4.54	4.26E-40
			CPT1B	3.44	5.78E-17
Non-alcoholic fatty liver disease (hsa04932)	151	6 (1/5)	IL1A	5.33	3.21E-24
			XBP1	2.64	2.05E-31
			IL1B	3.69	2.14E-07
			DDIT3	2.06	2.69E-06
			IFI30 // PIK3R2	2.00	1.12E-09
			CYP2E1	6.03	2.94E-15
Estrogen signaling pathway (hsa04915)	99	5 (4/1)	CREB5	2.59	1.24E-08
			GABBR2	2.42	8.04E-11
			PLCB4	2.49	1.32E-11
			HSPA6	2.58	6.61E-04
			IFI30 // PIK3R2	2.00	1.12E-09
Legionellosis (hsa05134)	54	4 (1/3)	CD14	2.92	2.97E-09
			IL1B	3.69	2.14E-07
			HSPA6	2.58	6.61E-04
			C3	2.27	7.66E-12
Measles (hsa05162)	133	4 (0/4)	TNFRSF10D	2.50	1.65E-08
			IFI30 // PIK3R2	2.00	1.12E-09
			IL1B	3.69	2.14E-07
			IL1A	5.33	3.21E-24
PI3K-Akt signaling pathway (hsa04151)	345	9 (6/3)	GNB3	6.68	2.97E-21
			OSM	2.24	9.51E-12
			VEGFC	2.13	2.41E-10
			PCK2	2.03	3.40E-14
			COL27A1	3.89	1.74E-29
			IFI30 // PIK3R2	2.00	1.12E-09
			L3MBTL1 // SGK2	6.90	2.97E-28
			CREB5	2.59	1.24E-08
			LAMA3	2.82	1.15E-23

D

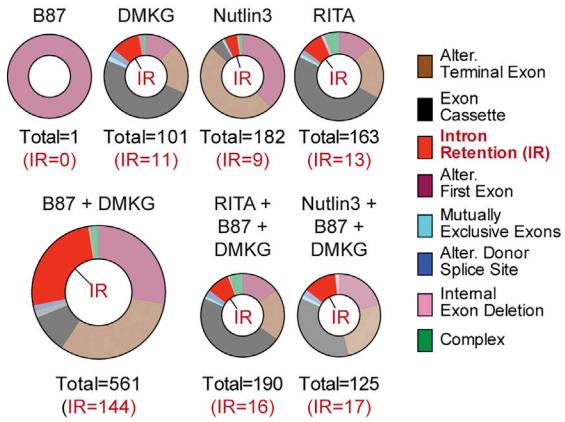

E

KEGG_PATHWAY	Count	PValue	Genes
hsa04141:Protein processing in endoplasmic reticulum	18	0.0001	HERPUD1, TUSC3, MBTPS2, HSP90AA1, UFD1L, UBE2G2, DNAJC10, CAPN2, CAPN1, UBE2E3, UBE2D3, ATF4, BAG1, ATF6B, DNAJB1, SSR4, HSPA8, SSR2
hsa03050:Proteasome	8	0.0009	PSMA1, PSMD13, PSMB1, PSMD11, PSME2, PSME4, PSMD6, PSMD8
hsa03040:Spliceosome	13	0.003	U2AF1L5, TRA2B, HNRNPU, SRSF2, TCERG1, AQR, DHX15, U2AF1, DHX16, THOC2, HSPA8, RBM25, DDX42
hsa03013:RNA transport	15	0.0037	ELAC2, EEF1A2, FMR1, PABPC4, EIF5, NUP85, RANGAP1, UBE2I, RNPS1, CASC3, NXF1, EIF3B, AAAS, THOC2, PABPC1L
hsa00010:Glycolysis / Gluconeogenesis	8	0.0102	ALDH7A1, PFKL, ADPGK, PDHA1, GAPDH, ALDH3B1, ALDH3A1, ENO1, HK1
hsa03015:mRNA surveillance pathway	9	0.0168	PPP2CA, NUDT21, PABPC4, PELO, RNPS1, NXF1, CASC3, PABPC1L, PPP2R2A
hsa04066:HIF-1 signaling pathway	9	0.0251	LTBR, MAP2K2, VEGFA, MKNK2, PDHA1, MTOR, GAPDH, PIK3R1, ENO1
hsa04910:Insulin signaling pathway	11	0.0276	SREBF1, CBLB, EXOC7, PTPRF, MAP2K2, PRKAG2, TSC2, PRKAR1A, MKNK2, MTOR, PIK3R1
hsa05169:Epstein-Barr virus infection	13	0.0424	PSMD13, PSMD11, IL10RB, VIM, CSNK2B, TAB1, PSMD6, NCOR2, PSMD8, TBPL1, POLR2B, PIK3R1, HSPA8

(legend on next page)

consumption in response to B87 (Figures S7E and S7F), yet recovered glycolysis even in the presence of B87 plus DMKG (Figures S7G and S7H). In addition, such resistant cells expressed lower amounts of APEX1, IDH1, PARP1, and SIRT1 proteins (Figure S7I) as well as lower mRNA levels of *MDM2* than their parental counterparts (Figure S7J).

Altogether, these results reinforce the notion that the combination of B87 plus DMKG kills susceptible cancer cells through a pathway that involves glycolysis inhibition as well as a series of atypical cell death effectors.

DISCUSSION

Here, we report on a synthetic lethality affecting cancer cells that are subjected to the simultaneous inhibition of mitochondrial respiration with B87 (or other OXPHOS inhibitors) and the addition of DMKG. B87 has originally been discovered as an inhibitor of hypoxia inducible factor 1 alpha (HIF1A; best known as HIF-1α), to which multiple tumors are addicted for surviving in the adverse conditions that normally characterize the tumor microenvironment (e.g., hypoxia, limited nutrient availability) (LaGory and Giaccia, 2016; Masson and Ratcliffe, 2014). Interestingly, B87 was shown to inhibit respiratory complex I with exquisite efficacy (Ellinghaus et al., 2013). Most likely, such an inhibitory effect (which precludes oxygen consumption by mitochondria) accounts for an increase in local oxygen concentration and consequent HIF-1α inhibition. Importantly, αKG, the active metabolite of DMKG, is an obligatory cofactor of prolyl-hydroxylases (Tennant and Gottlieb, 2010), meaning that an elevation in intracellular αKG availability might contribute to HIF-1α degradation as well. However, HIF-1α target genes were not particularly depleted (and *VEGFC* was actually upregulated) by B87 plus DMKG, suggesting that HIF-1α inhibition alone cannot account for the lethal effects of this combined regimen.

A panel of rather distinct cancer cell lines maintained in standard culture conditions (normoxia and normal nutrient availability) were killed by B87 plus DMKG, contrasting with the resistance of several non-transformed cell lines, perhaps reflecting tumor-cell-specific metabolic circuitries (Altman et al., 2016; Galluzzi et al., 2013). It should be noted that, in our hands, B87 employed as a stand-alone therapeutic intervention inhibited the proliferation of human carcinoma and lung cancer cells, but failed to promote cell death. Only when combined with DMKG, B87 (or any other OXPHOS inhibitor), caused rapid cell killing.

The combination of B87 and DMKG kills cancer cells through transcriptional reprogramming, leading to a major alteration in gene expression profiles and alternative splicing. In particular, these transcriptional effects could be reversed by the addition of two chemically unrelated MDM2 inhibitors: RITA and Nutlin3. Although MDM2 is best known as a negative regulator of TP53 (Bohlman and Manfredi, 2014; Kubbutat et al., 1997), TP53 is not involved in the cytotoxicity of B87 plus DMKG, suggesting that MDM2 must act on other transcription factors (or itself mediate transcriptional effects) (Riscal et al., 2016) to participate in this lethal signaling pathway. In accord with this possibility, MDM2 was found to translocate to the nucleus in the presence of B87 plus DMKG. Multiple genes involved in biosynthetic reactions (RNA splicing, mRNA surveillance, RNA transport and protein processing) were affected by the alternative splicing events triggered by B87 plus DMKG (and reversed by MDM2 inhibitors), suggesting a profound remodeling of RNA and protein processing. In addition, alternative exon usage affected a host of genes involved in insulin signaling and glucose metabolism. This latter effect appears to be functionally relevant because glycolysis is suppressed by B87 plus DMKG (but not by the compounds alone). Disabled glycolysis was detected by several complementary technologies, namely, the measurement of ECAR, mass spectrometric metabolomics, fluxomics of ^{13}C-glucose catabolism, as well as by biosensor-based measurements of pyruvate influx into mitochondria. Although glucose uptake into cells exposed to B87 plus DMKG was normal, the very first step in glycolysis, namely the phosphorylation of glucose to glucose-6-phosphate, was inhibited, correlating with the fact that hexokinase 1 (*HXK1*), which codes for the enzyme catalyzing this reaction, was affected by alternative exon usage. Nutlin3 and RITA re-established glycolytic flux at all levels as they normalized most of the transcriptional changes induced by B87 plus DMKG, especially at the level of exon usage. Moreover, the capacity of MDM2 inhibitors to suppress the cytotoxic effect of B87 plus DMKG depended on the reestablishment of glycolysis, as demonstrated by the fact that inhibition of HXK by 2DG compromised the cytoprotective action of Nutlin3 and RITA.

The bioenergetic crisis caused by B87 plus DMKG originates from the simultaneous inhibition of oxidative phosphorylation (upon complex I inhibition by B87) and glycolysis (a consequence of the transcriptional effects of B87 and DMKG), leading to a synergistic cytotoxic interaction. DMKG must be metabolized to isocitrate to mediate synthetic lethality with B87, because knockdown of IDH1, the cytosolic enzyme that converts αKG (the de-esterification product of DMKG) to isocitrate,

Figure 6. RITA or Nutlin3 Reverse the Transcriptional Effects of Dimethyl α-Ketoglutarate plus B87

(A) H460 cells were treated with DMKG, B87 alone, or in combination, optionally together with actinomycin D (ActD) or cycloheximide (CHX). Afterward, the treatments cells were collected and double stained with PI and $DiOC_6(3)$ for the cytofluorimetric detection of dying ($DiOC_6(3)^{low}$ PI^-) and dead (PI^+) cells. n = 3.

(B) Heatmap representing the most-altered transcripts detected by the RNA-sequencing analysis, in H460 cells treated with DMKG plus B87 with or without MDM2 inhibitors. n = 4.

(C) KEGG pathway analysis of the transcripts represented in (B). Fold change and p value refer to the comparison with the untreated cells. n = 4.

(D) Distribution of alternative splicing event types affecting exon usage, based on pattern analyses of the indicated treatments compared to untreated cells. The number of intron retention (IR) events in the different treatments compared to the control is indicated. n = 4.

(E) KEGG pathway analysis of the genes affected by alternative exon usage upon DMKG plus B87 treatment. n = 4.

Symbols indicate significant (unpaired Student's t test) changes with respect to controls (***$p < 0.001$) or to B87 plus DMKG ($^{\$\$\$}p < 0.001$). Columns indicate means ± SD. The figures are representative of three independent experiments yielding similar results.

Drug concentrations and times of treatments are detailed in Table S6.

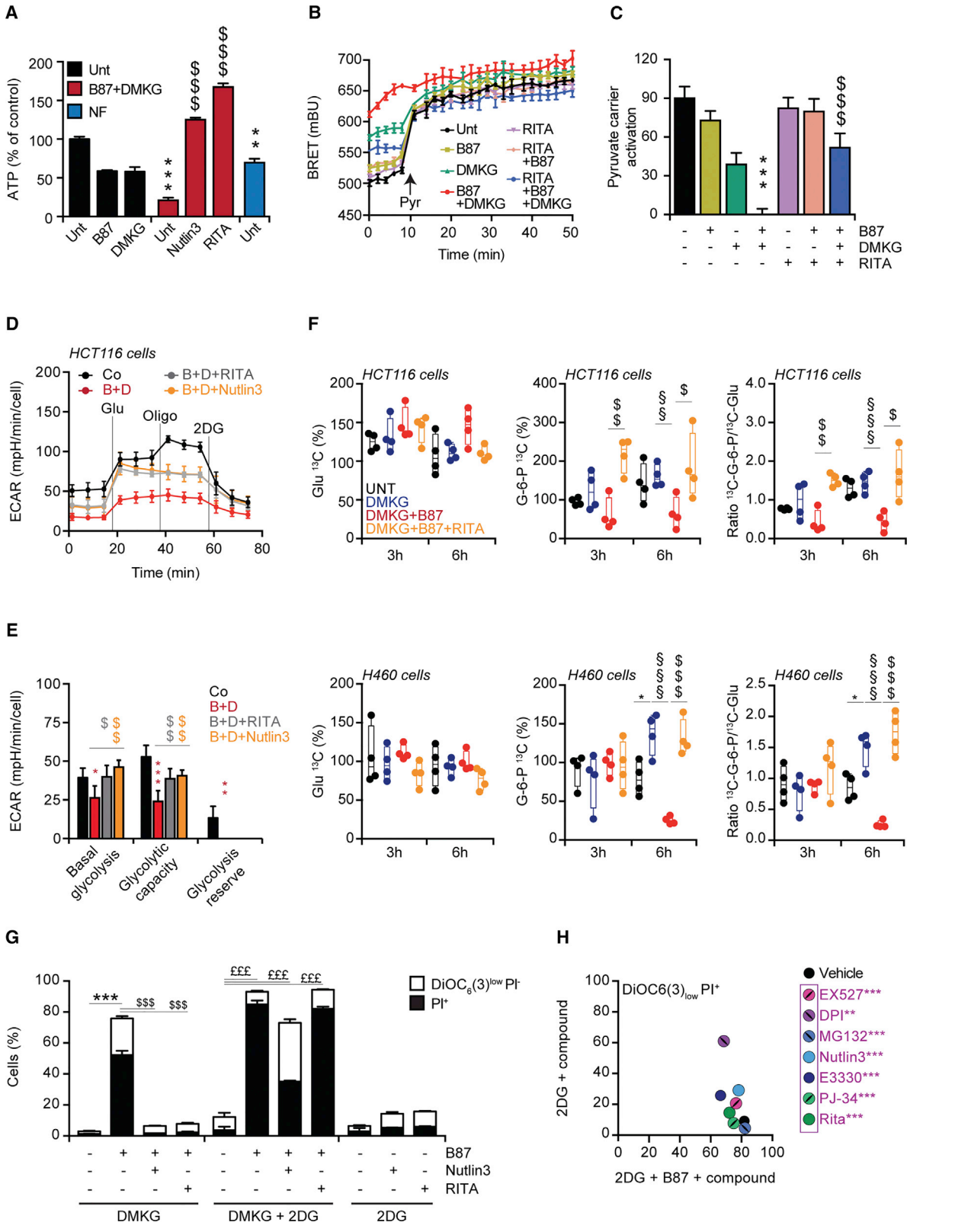

(legend on next page)

attenuated cell killing by B87 plus DMKG. However, it remains to be determined which metabolites downstream of isocitrate participate in the effects of DMKG. Thus, complex changes in the metabolome are likely to contribute to the cytotoxic action of the combination treatment.

B87 plus DMKG failed to induce morphological hallmarks of apoptosis, and inhibition of caspases did not delay cell killing. Similarly, the simultaneous administration of B87 and DMKG failed to induce morphological signs of autophagy. Autophagy inhibition, however, had no major role in the lethal action of B87 plus DMKG, because knocking down essential autophagy gene products (such as ATG5 or ATG7) was not sufficient to kill cells when treated with either B87 or DMKG alone (not shown). Rather, inhibition of autophagy may have occurred as a result of ATP depletion, since ATP is required for several steps of the autophagic process (Nath et al., 2014). Moreover, inhibition of enzymes involved in necroptosis or ferroptosis, as well as high doses of antioxidants, failed to convey cytoprotection against B87 plus DMKG. Instead, the combination of B87 and DMKG was able to disrupt the mitochondrial network, an alteration that appears to be linked to RCD induction and that was prevented by RITA and Nutlin3. Moreover, several proteins involved in parthanatos, a cell death modality that has mostly been involved in ischemia reperfusion damage of the central nervous system (Andrabi et al., 2008), contribute to cell killing by B87 plus DMKG. This applies to PARP1 and AIFM1, two central mediators of parthanatos. Beyond these factors, the endonuclease APEX1 and its activator SIRT1 may contribute to the cytotoxic effects of B87 plus DMKG. Thus, pharmacological or genetic suppression of PARP1, AIFM1, APEX1, or SIRT1 can rescue cells from B87 and DMKG-driven RCD. Hence, the activation of a number of cellular enzymes and the degradation of proteins like HSP70 (Mosser et al., 1997) and FOXO1 (Fu et al., 2009), which are fundamental in protecting cells from stress stimuli, appear to contribute to cell killing downstream of the bioenergetic catastrophe provoked by simultaneous inhibition of oxidative phosphorylation and glycolysis. Moreover, RITA and Nutlin3, two inhibitors of the MDM2-TP53 interaction, efficiently inhibit B87 plus DMKG RCD and MDM2 translocation to the nucleus. These findings raise interesting question regarding the mechanism of action of these two inhibitors, suggesting the existence of yet-to-be-explored TP53-independent MDM2-associated functions.

The aforementioned cascade of molecular events (transcriptional reprogramming downstream of MDM2, inhibition of glycolysis within the context of suppressed oxidative phosphorylation, activation of RCD) appears complex, perhaps reflecting the normal resilience of transformed cells against lethal manipulations. Apparently, it is only a combined intervention on several metabolic pathways that may trigger cancer cell death. Irrespective of this speculation, however, it appears that DMKG coupled with inhibitors of oxidative phosphorylation has a relatively broad cytotoxic impact on different cancer cell types that may be used to reduce tumor growth in preclinical models.

STAR★METHODS

Detailed methods are provided in the online version of this paper and include the following:

- KEY RESOURCES TABLE
- CONTACT FOR REAGENT AND RESOURCE SHARING
- EXPERIMENTAL MODEL AND SUBJECT DETAILS
  - Mammalian cell lines
  - Mouse model
- METHODS DETAILS
  - BAY 87-2243
  - RNA interference
  - Plasmid transfection
  - Oxygen consumption
  - Glycolytic flux
  - Real time video
  - Cytofluorometric assessment of apoptosis and cell cycle distribution
  - Transmission electron microscopy
  - Immunofluorescence
  - Sample preparation for metabolomics analysis
  - Untargeted metabolomics analysis of intracellular metabolites by UHPLC coupled to a quadrupole-time of flight (QTOF) mass spectrometer

Figure 7. MDM2 Inhibitors Rescue the Glycolytic Defect Induced by Dimethyl α-Ketoglutarate plus B87

(A) Measurement of intracellular ATP upon treatments indicated, in H460 cells. Nutrient free (NF) treatment was used as a positive control of ATP depletion. $n \geq 3$.

(B and C) Mitochondrial pyruvate carrier activity.

(B) Bioluminescence resonance energy transfer (BRET) kinetics was measured in H460 cells stably expressing MPC1-Venus and MPC2-RLuc8. Cells were pretreated as indicated and an injection of pyruvate (Pyr) occurred at the time indicated by the arrow.

(C) Histograms representing V_{max} of the curves after Pyr injection. n = 4.

(D and E) HCT116 cells were cultured in specialized XF-96-well plates and treated as indicated, then analyzed by a Seahorse apparatus (D) to measure glycolysis by means of the extracellular acidification rate (ECAR) (E). B, B87; D, DMKG; Glu, Glucose; Oligo, Oligomycin A; and 2DG, 2-deoxyglucose. n = 5.

(F) Glycolysis flux measurement. Mass spectrometry in H460 and HCT116 cell lines receiving ^{13}C-glucose alone or together with indicated treatments was used to detect ^{13}C-glucose and ^{13}C-glucose-6-phosphate (all carbons labeled) after 3-h and 6-h treatments. G-6-P, Glucose-6-phosphate. n = 4.

(G) H460 cells were treated with DMKG, 2DG, or in combination, optionally together with B87 in the presence or absence of RITA or Nutlin3. Cells were collected and double stained with PI and $DiOC_6(3)$ for the cytofluorimetric detection of dying ($DiOC_6(3)^{low}$ PI^-) and dead (PI^+) cells. n = 3.

(H) H460 cells were treated with 2DG or in combination with B87, optionally together with the compounds listed. After the treatments, cells were collected and analyzed as in (G). n = 3.

Symbols indicate significant (unpaired Student's t test) changes with respect to controls (*$p < 0.05$, **$p < 0.01$ and ***$p < 0.001$), to B87 ($^{§§}p < 0.01$ and $^{§§§}p < 0.001$), to B87 plus DMKG ($^{\$}p < 0.05$, $^{\$\$}p < 0.01$, and $^{\$\$\$}p < 0.001$), or DMKG plus 2DG ($^{£££}p < 0.001$). Columns indicate means ± SD (A, C, E, and G) or box-and-whisker plots (mean, first and third quartiles, and maximum and minimum values) (F). The figures are representative of three independent experiments yielding similar results.

Drugs concentration and time of treatments are detailed in Tables S5 and S6.

- Targeted analysis of intracellular metabolites by UHPLC coupled to a Triple Quadrupole (QQQ) mass spectrometer
- Fluxomic analysis
- Intracellular ATP assessment
- Immunoblotting
- Carboxyfluorescein succinimidyl ester (CFSE) staining
- *In vivo* experiments
- Gene expression analysis
- RNA-sequencing
- RNA-seq data analysis
- Unsupervised analysis
- Pathway/Gene Ontology (GO) analysis and transcription factor analysis
- Monitoring mitochondrial pyruvate carrier activity

- QUANTIFICATION AND STATISTICAL ANALYSIS
- DATA AND SOFTWARE AVAILABILITY

SUPPLEMENTAL INFORMATION

Supplemental Information can be found online at https://doi.org/10.1016/j.celrep.2019.03.058.

ACKNOWLEDGMENTS

We thank Bert Vogelstein (The John Hopkins University, Baltimore, MD, USA) for p53-deficient cells, Carlos López Otín for critical reading of the manuscript, the CRC core facilities for technical support, and Nicolas Signolle, Paule Opolon, and Olivia Bawa from the facility "Pathologie expérimentale et translationnelle." L.G. is supported by a startup grant from the Department of Radiation Oncology at Weill Cornell Medical College (New York, NY, USA) and from Sotio a.s. (Prague, Czech Republic). G.K. is supported by the Ligue contre le Cancer Comité de Charente-Maritime (équipe labelisée); Agence National de la Recherche (ANR) – Projets blancs; ANR under the frame of E-Rare-2, the ERA-Net for Research on Rare Diseases; Association pour la recherche sur le cancer (ARC); Cancéropôle Ile-de-France; Chancelerie des universités de Paris (Legs Poix), Fondation pour la Recherche Médicale (FRM); the European Commission (ArtForce); the European Research Council (ERC); Fondation Carrefour; Institut National du Cancer (INCa); INSERM (HTE); Institut Universitaire de France; LeDucq Foundation; the LabEx Immuno-Oncology; the RHU Torino Lumière; the Searave Foundation; the SIRIC Stratified Oncology Cell DNA Repair and Tumor Immune Elimination (SOCRATE); the SIRIC Cancer Research and Personalized Medicine (CARPEM); and the Paris Alliance of Cancer Research Institutes (PACRI).

AUTHOR CONTRIBUTIONS

V.S. and J.M.B.-S.P. performed most of the experiments. M.C.M. and V.I. contributed to *in vitro* and *in vivo* experiments. J.P. contributed to *in vivo* experiments. E.V., S.P., and J.-C.M. performed RESPYR experiments and analysis. D.E., S.D., N.B., and A.C. performed metabolomic experiments. S.S. and G.P. performed TEM experiments. A.S. and O.K. performed and analyzed chemotherapeutic drug screenings. L.M. generated HCT116 *AIFM1*$^{-/-}$ cells. N.Z., T.S., L.G., H.H.-S., and K.Z. helped with data interpretation. V.S., J.M.B.-S.P., M.C.M., and G.K. conceived the study, interpreted the data, and wrote the manuscript.

DECLARATION OF INTERESTS

This study was supported by a grant from Bayer Pharma AG. H.H.-S. and K.Z. are full-time employees of Bayer Pharma. G.K. operates as an independent consultant for Bayer Pharma.

Received: June 28, 2018
Revised: January 25, 2019
Accepted: March 15, 2019
Published: April 16, 2019

REFERENCES

Altman, B.J., Stine, Z.E., and Dang, C.V. (2016). From Krebs to clinic: glutamine metabolism to cancer therapy. Nat. Rev. Cancer *16*, 749.

Andrabi, S.A., Dawson, T.M., and Dawson, V.L. (2008). Mitochondrial and nuclear cross talk in cell death: parthanatos. Ann. N Y Acad. Sci. *1147*, 233–241.

Antoniali, G., Lirussi, L., D'Ambrosio, C., Dal Piaz, F., Vascotto, C., Casarano, E., Marasco, D., Scaloni, A., Fogolari, F., and Tell, G. (2014). SIRT1 gene expression upon genotoxic damage is regulated by APE1 through nCaRE-promoter elements. Mol. Biol. Cell *25*, 532–547.

Bálint, E., Bates, S., and Vousden, K.H. (1999). Mdm2 binds p73 alpha without targeting degradation. Oncogene *18*, 3923–3929.

Bohlman, S., and Manfredi, J.J. (2014). p53-independent effects of Mdm2. Subcell. Biochem. *85*, 235–246.

Bunz, F., Hwang, P.M., Torrance, C., Waldman, T., Zhang, Y., Dillehay, L., Williams, J., Lengauer, C., Kinzler, K.W., and Vogelstein, B. (1999). Disruption of p53 in human cancer cells alters the responses to therapeutic agents. J. Clin. Invest. *104*, 263–269.

Busso, C.S., Iwakuma, T., and Izumi, T. (2009). Ubiquitination of mammalian AP endonuclease (APE1) regulated by the p53-MDM2 signaling pathway. Oncogene *28*, 1616–1625.

Chen, D., Li, M., Luo, J., and Gu, W. (2003). Direct interactions between HIF-1 alpha and Mdm2 modulate p53 function. J. Biol. Chem. *278*, 13595–13598.

Compan, V., Pierredon, S., Vanderperre, B., Krznar, P., Marchiq, I., Zamboni, N., Pouyssegur, J., and Martinou, J.C. (2015). Monitoring mitochondrial pyruvate carrier activity in real time using a BRET-based biosensor: investigation of the Warburg effect. Mol. Cell *59*, 491–501.

Deeks, E.D. (2016). Venetoclax: First Global Approval. Drugs *76*, 979–987.

Dobin, A., Davis, C.A., Schlesinger, F., Drenkow, J., Zaleski, C., Jha, S., Batut, P., Chaisson, M., and Gingeras, T.R. (2013). STAR: ultrafast universal RNA-seq aligner. Bioinformatics *29*, 15–21.

Ellinghaus, P., Heisler, I., Unterschemmann, K., Haerter, M., Beck, H., Greschat, S., Ehrmann, A., Summer, H., Flamme, I., Oehme, F., et al. (2013). BAY 87-2243, a highly potent and selective inhibitor of hypoxia-induced gene activation has antitumor activities by inhibition of mitochondrial complex I. Cancer Med. *2*, 611–624.

Fogal, V., Richardson, A.D., Karmali, P.P., Scheffler, I.E., Smith, J.W., and Ruoslahti, E. (2010). Mitochondrial p32 protein is a critical regulator of tumor metabolism via maintenance of oxidative phosphorylation. Mol. Cell. Biol. *30*, 1303–1318.

Fu, W., Ma, Q., Chen, L., Li, P., Zhang, M., Ramamoorthy, S., Nawaz, Z., Shimojima, T., Wang, H., Yang, Y., et al. (2009). MDM2 acts downstream of p53 as an E3 ligase to promote FOXO ubiquitination and degradation. J. Biol. Chem. *284*, 13987–14000.

Fulda, S., Galluzzi, L., and Kroemer, G. (2010). Targeting mitochondria for cancer therapy. Nat. Rev. Drug Discov. *9*, 447–464.

Galluzzi, L., Larochette, N., Zamzami, N., and Kroemer, G. (2006). Mitochondria as therapeutic targets for cancer chemotherapy. Oncogene *25*, 4812–4830.

Galluzzi, L., Kepp, O., Vander Heiden, M.G., and Kroemer, G. (2013). Metabolic targets for cancer therapy. Nat. Rev. Drug Discov. *12*, 829–846.

Green, D.R., and Reed, J.C. (1998). Mitochondria and apoptosis. Science *281*, 1309–1312.

Green, D.R., Galluzzi, L., and Kroemer, G. (2014). Cell biology. Metabolic control of cell death. Science *345*, 1250256.

Helbig, L., Koi, L., Brüchner, K., Gurtner, K., Hess-Stumpp, H., Unterschemmann, K., Baumann, M., Zips, D., and Yaromina, A. (2014). BAY 87-2243, a novel inhibitor of hypoxia-induced gene activation, improves local tumor

control after fractionated irradiation in a schedule-dependent manner in head and neck human xenografts. Radiat. Oncol. *9*, 207.

Juven-Gershon, T., Shifman, O., Unger, T., Elkeles, A., Haupt, Y., and Oren, M. (1998). The Mdm2 oncoprotein interacts with the cell fate regulator Numb. Mol. Cell. Biol. *18*, 3974–3982.

Kisselev, A.F., and Goldberg, A.L. (2001). Proteasome inhibitors: from research tools to drug candidates. Chem. Biol. *8*, 739–758.

Kroemer, G., and Reed, J.C. (2000). Mitochondrial control of cell death. Nat. Med. *6*, 513–519.

Kubbutat, M.H., Jones, S.N., and Vousden, K.H. (1997). Regulation of p53 stability by Mdm2. Nature *387*, 299–303.

LaGory, E.L., and Giaccia, A.J. (2016). The ever-expanding role of HIF in tumour and stromal biology. Nat. Cell Biol. *18*, 356–365.

Lapointe, N., St-Hilaire, M., Martinoli, M.G., Blanchet, J., Gould, P., Rouillard, C., and Cicchetti, F. (2004). Rotenone induces non-specific central nervous system and systemic toxicity. FASEB J. *18*, 717–719.

Lee, J.H., Budanov, A.V., and Karin, M. (2013). Sestrins orchestrate cellular metabolism to attenuate aging. Cell Metab. *18*, 792–801.

Liang, Y., Zhu, J., Huang, H., Xiang, D., Li, Y., Zhang, D., Li, J., Wang, Y., Jin, H., Jiang, G., et al. (2016). SESN2/sestrin 2 induction-mediated autophagy and inhibitory effect of isorhapontigenin (ISO) on human bladder cancers. Autophagy *12*, 1229–1239.

Love, M.I., Huber, W., and Anders, S. (2014). Moderated estimation of fold change and dispersion for RNA-seq data with DESeq2. Genome Biol. *15*, 550.

Maddocks, O.D.K., Athineos, D., Cheung, E.C., Lee, P., Zhang, T., van den Broek, N.J.F., Mackay, G.M., Labuschagne, C.F., Gay, D., Kruiswijk, F., et al. (2017). Modulating the therapeutic response of tumours to dietary serine and glycine starvation. Nature *544*, 372–376.

Mariño, G., Pietrocola, F., Eisenberg, T., Kong, Y., Malik, S.A., Andryushkova, A., Schroeder, S., Pendl, T., Harger, A., Niso-Santano, M., et al. (2014). Regulation of autophagy by cytosolic acetyl-coenzyme A. Mol. Cell *53*, 710–725.

Martin, K., Trouche, D., Hagemeier, C., Sørensen, T.S., La Thangue, N.B., and Kouzarides, T. (1995). Stimulation of E2F1/DP1 transcriptional activity by MDM2 oncoprotein. Nature *375*, 691–694.

Masson, N., and Ratcliffe, P.J. (2014). Hypoxia signaling pathways in cancer metabolism: the importance of co-selecting interconnected physiological pathways. Cancer Metab. *2*, 3.

Mikawa, T., Maruyama, T., Okamoto, K., Nakagama, H., Lleonart, M.E., Tsusaka, T., Hori, K., Murakami, I., Izumi, T., Takaori-Kondo, A., et al. (2014). Senescence-inducing stress promotes proteolysis of phosphoglycerate mutase via ubiquitin ligase Mdm2. J. Cell Biol. *204*, 729–745.

Mosser, D.D., Caron, A.W., Bourget, L., Denis-Larose, C., and Massie, B. (1997). Role of the human heat shock protein hsp70 in protection against stress-induced apoptosis. Mol. Cell. Biol. *17*, 5317–5327.

Nath, S., Dancourt, J., Shteyn, V., Puente, G., Fong, W.M., Nag, S., Bewersdorf, J., Yamamoto, A., Antonny, B., and Melia, T.J. (2014). Lipidation of the LC3/GABARAP family of autophagy proteins relies on a membrane-curvature-sensing domain in Atg3. Nat. Cell Biol. *16*, 415–424.

Noli, L., Capalbo, A., Ogilvie, C., Khalaf, Y., and Ilic, D. (2015). Discordant growth of monozygotic twins starts at the blastocyst stage: a case study. Stem Cell Reports *5*, 946–953.

Riscal, R., Schrepfer, E., Arena, G., Cissé, M.Y., Bellvert, F., Heuillet, M., Rambow, F., Bonneil, E., Sabourdy, F., Vincent, C., et al. (2016). Chromatin-bound MDM2 regulates serine metabolism and redox homeostasis independently of p53. Mol. Cell *62*, 890–902.

Roberts, A.W., Davids, M.S., Pagel, J.M., Kahl, B.S., Puvvada, S.D., Gerecitano, J.F., Kipps, T.J., Anderson, M.A., Brown, J.R., Gressick, L., et al. (2016). Targeting BCL2 with venetoclax in relapsed chronic lymphocytic leukemia. N. Engl. J. Med. *374*, 311–322.

Schöckel, L., Glasauer, A., Basit, F., Bitschar, K., Truong, H., Erdmann, G., Algire, C., Hägebarth, A., Willems, P.H., Kopitz, C., et al. (2015). Targeting mitochondrial complex I using BAY 87-2243 reduces melanoma tumor growth. Cancer Metab. *3*, 11.

Shen, H., and Maki, C.G. (2011). Pharmacologic activation of p53 by small-molecule MDM2 antagonists. Curr. Pharm. Des. *17*, 560–568.

Sica, V., Manic, G., Kroemer, G., Vitale, I., and Galluzzi, L. (2016). Cytofluorometric quantification of cell death elicited by NLR proteins. Methods Mol. Biol. *1417*, 231–245.

Sica, V., Bravo-San Pedro, J.M., Pietrocola, F., Izzo, V., Maiuri, M.C., Kroemer, G., and Galluzzi, L. (2017). Assessment of glycolytic flux and mitochondrial respiration in the course of autophagic responses. Methods Enzymol. *588*, 155–170.

Souers, A.J., Leverson, J.D., Boghaert, E.R., Ackler, S.L., Catron, N.D., Chen, J., Dayton, B.D., Ding, H., Enschede, S.H., Fairbrother, W.J., et al. (2013). ABT-199, a potent and selective BCL-2 inhibitor, achieves antitumor activity while sparing platelets. Nat. Med. *19*, 202–208.

Srivastava, P., and Panda, D. (2007). Rotenone inhibits mammalian cell proliferation by inhibiting microtubule assembly through tubulin binding. FEBS J. *274*, 4788–4801.

Tennant, D.A., and Gottlieb, E. (2010). HIF prolyl hydroxylase-3 mediates alpha-ketoglutarate-induced apoptosis and tumor suppression. J. Mol. Med. (Berl.) *88*, 839–849.

Torrance, C.J., Jackson, P.E., Montgomery, E., Kinzler, K.W., Vogelstein, B., Wissner, A., Nunes, M., Frost, P., and Discafani, C.M. (2000). Combinatorial chemoprevention of intestinal neoplasia. Nat. Med. *6*, 1024–1028.

Vitale, I., Jemaà, M., Galluzzi, L., Metivier, D., Castedo, M., and Kroemer, G. (2013). Cytofluorometric assessment of cell cycle progression. Methods Mol. Biol. *965*, 93–120.

Wallace, D.C. (2012). Mitochondria and cancer. Nat. Rev. Cancer *12*, 685–698.

Way, L., Faktor, J., Dvorakova, P., Nicholson, J., Vojtesek, B., Graham, D., Ball, K.L., and Hupp, T. (2016). Rearrangement of mitochondrial pyruvate dehydrogenase subunit dihydrolipoamide dehydrogenase protein-protein interactions by the MDM2 ligand nutlin-3. Proteomics *16*, 2327–2344.

Weinberg, F., Hamanaka, R., Wheaton, W.W., Weinberg, S., Joseph, J., Lopez, M., Kalyanaraman, B., Mutlu, G.M., Budinger, G.R., and Chandel, N.S. (2010). Mitochondrial metabolism and ROS generation are essential for Kras-mediated tumorigenicity. Proc. Natl. Acad. Sci. USA *107*, 8788–8793.

Wheaton, W.W., Weinberg, S.E., Hamanaka, R.B., Soberanes, S., Sullivan, L.B., Anso, E., Glasauer, A., Dufour, E., Mutlu, G.M., Budigner, G.S., and Chandel, N.S. (2014). Metformin inhibits mitochondrial complex I of cancer cells to reduce tumorigenesis. eLife *3*, e02242.

Wolinsky, J.B., Colson, Y.L., and Grinstaff, M.W. (2012). Local drug delivery strategies for cancer treatment: gels, nanoparticles, polymeric films, rods, and wafers. J. Control. Release *159*, 14–26.

Yamamori, T., DeRicco, J., Naqvi, A., Hoffman, T.A., Mattagajasingh, I., Kasuno, K., Jung, S.B., Kim, C.S., and Irani, K. (2010). SIRT1 deacetylates APE1 and regulates cellular base excision repair. Nucleic Acids Res. *38*, 832–845.

STAR★METHODS

KEY RESOURCES TABLE

REAGENT or RESOURCE	SOURCE	IDENTIFIER
Antibodies		
Mouse monoclonal anti-SQSTM1	Abnova	Cat# H00008878-M01; RRID: AB_548364
Rabbit polyclonal anti-LC3B	Cell Signaling Technology	Cat#2775; RRID: AB_915950
Mouse monoclonal anti-MDM2	Santa Cruz Biotechnology	Cat#sc-965; RRID: AB_627920
Rabbit polyclonal anti-PARP1	Cell signaling Technology	Cat#9542; RRID: AB_2160739
Rabbit monoclonal anti-IDH1	Cell Signaling Technology	Cat#8137; RRID: AB_10950504
Mouse monoclonal anti-TP53	Cell Signaling Technology	Cat#48818; RRID: AB_2713958
Rabbit polyclonal anti-AIFM1	Cell Signaling Technology	Cat#4642; RRID: AB_2224542
Mouse monoclonal anti-APEX1	Santa Cruz Biotechnology	Cat#sc-17774; RRID: AB_626685
Rabbit polyclonal anti-SIRT1	Abcam	Cat#ab7343; RRID: AB_305867
Rabbit polyclonal anti-Ubiquitin	Abcam	Cat#ab7780; RRID: AB_306069
Rabbit monoclonal anti-FOXO1	Cell Signaling Technology	Cat#2880; RRID: AB_2106495
Rabbit polyclonal anti-HSP70	Cell Signaling Technology	Cat#4872; RRID: AB_2279841
Mouse monoclonal anti-GAPDH	Abcam	Cat#ab9484; RRID: AB_307274
Mouse monoclonal anti-β−actin	Abcam	Cat#ab20272; RRID: AB_445482
Mouse monoclonal anti-Myc-Tag	Cell Signaling Technology	Cat#2276; RRID: AB_331783
Rabbit monoclonal anti-Lamin B1	Cell Signaling Technology	Cat#12586; RRID: AB_2650517
Mouse monoclonal anti-TIM23	BD Biosciences	Cat# 611223; RRID: AB_398755
Rabbit polyclonal anti-TOMM20	Santa Cruz Biotechnology	Cat# sc-11415; discontinued
Alexa Fluor 594 Phalloidin	Thermo Fisher Scientific	Cat# A12381
Chemicals, Peptides, and Recombinant Proteins		
BAY87-2243	Provided by Bayer	N/A
Dimethyl α−ketoglutarate	Sigma-Aldrich	Cat# 349631
α−ketoglutarate	Sigma-Aldrich	Cat# 75890
2-deoxyglucose	Sigma-Aldrich	Cat# D3179
ABT-737	SelleckChem	Cat# S1002
Actinomycin D	Sigma-Aldrich	Cat# A9415
Antimycin A	Sigma-Aldrich	Cat# A8674
Bafilomycin A1	Tocris	Cat# 1334
BEZ235	SelleckChem	Cat# S1009
Carbonyl cyanide m-chlorophenyl hydrazine	Sigma-Aldrich	Cat# C2759
CEP1	Cephalon	CEP 8983
Cycloheximide	Sigma-Aldrich	Cat# C1988
Cytochalasin B	Sigma-Aldrich	Cat# C6762
Sodium dichloroacetate	Sigma-Aldrich	Cat# 347795
Dimethyl Succinate	Sigma-Aldrich	Cat# W239607
Diphenylene iodonium	Sigma-Aldrich	Cat# D2926
Etomoxir	Sigma-Aldrich	Cat# 1905
EX527	Sigma-Aldrich	Cat# E7034
E3330	Sigma-Aldrich	Cat# E8534
Ferrostatin-1	Sigma-Aldrich	Cat# SML0583
Glucose	Sigma-Aldrich	Cat# G7021
Glutamine	GIBCO-Life Tech	Cat# A2916801

(*Continued on next page*)

Continued

REAGENT or RESOURCE	SOURCE	IDENTIFIER
Glutathione reduced, ethyl ester	Sigma-Aldrich	Cat# G1404
GSK1059615	SelleckChem	Cat# S1360
Hydroxychloroquine (Lys05)	Sigma-Aldrich	Cat# SML2097
Potassium hydroxycitrate	Sigma-Aldrich	Cat# 59847
α-ketoisocaproic acid	Sigma-Aldrich	Cat# K0629
Lipoic acid	Sigma-Aldrich	Cat# T1395
Menadione	Sigma-Aldrich	Cat# M2518
Metformin	Sigma-Aldrich	Cat# D150959
MG132	Tocris	Cat# 1748
N-acetyl cysteine	Sigma-Aldrich	Cat# A9165
Necrostatin-1	Sigma-Aldrich	Cat# N9037
Nicotinamide	Sigma-Aldrich	Cat# N0636
Nutlin3	Sigma-Aldrich	Cat# N6287
Oligomycin A	Sigma-Aldrich	Cat# 75351
Perifosine	Sigma-Aldrich	Cat# SML0612
Phenformin	Santa Cruz Biotechnology	Cat# sc-219590
Pifithrin-a	Sigma-Aldrich	Cat# P4359
PJ-34	Sigma-Aldrich	Cat# P4365
Pyruvate	GIBCO-Life Tech	Cat# 11360070
Reactivation of p53 and Induction of Tumor cell Apoptosis (RITA)	Tocris	Cat# 2443
Rotenone	Sigma-Aldrich	Cat# 557368
Staurosporine	Sigma-Aldrich	Cat# S5921
5-(tetradecyloxy)-2-furoic acid	Sigma-Aldrich	Cat# T6575
Thenoyltrifluoroacetone	Cayman chemical	Cat# 326-91-0
Torin 1	Tocris	Cat# 4247
Z-VAD-fmk	SelleckChem	Cat# S7023
Allopurinol	Sigma-Aldrich	Cat# A8003-5G
Altretamine	Sigma-Aldrich	Cat# 549835-25G
Aminolevulinic acid	Sigma-Aldrich	Cat# A7793-10MG
Anastrozole	Sigma-Aldrich	Cat# Y0001522-1EA
Arsenic trioxide	Sigma-Aldrich	Cat# 311383-125G
Azacitidine	Sigma-Aldrich	Cat# A2385-250MG
Bendamustine HCl	Sigma-Aldrich	Cat# B5437-5MG
Busulfan	Sigma-Aldrich	Cat# B2635-10G
Capecitabine	Sigma-Aldrich	Cat# SML0653-10MG
Carboplatin	Sigma-Aldrich	Cat# C2538-100MG
Carmustine	Sigma-Aldrich	Cat# C0400-25MG
Celecoxib	Sigma-Aldrich	Cat# Y0001445-1EA
Chlorambucil	Sigma-Aldrich	Cat# C0253-1G
Cisplatin	Sigma-Aldrich	Cat# C2210000-1EA
Cladribine	Sigma-Aldrich	Cat# Y0000639-1EA
Clofarabine	Sigma-Aldrich	Cat# C7495-5MG
Crizotinib	Sigma-Aldrich	Cat# PZ0191-5MG
Cyclophosphamide	Sigma-Aldrich	C3250000-1EA
Cytarabine HCl	Sigma-Aldrich	C6645-100MG
Dacarbazine	Sigma-Aldrich	Cat# Y0000733-1EA
Dactinomycin	Sigma-Aldrich	Cat# A1410-25MG

(*Continued on next page*)

Continued

REAGENT or RESOURCE	SOURCE	IDENTIFIER
Decitabine	Sigma-Aldrich	Cat# A3656-5MG
Dexrazoxone	Sigma-Aldrich	Cat# D1446-5MG
Docetaxel	Sigma-Aldrich	Cat# 01885-5MG-F
Estramustine disodium phosphate	Sigma-Aldrich	Cat# E0407-5MG
Etoposide	Sigma-Aldrich	Cat# E2600000-1EA
Everolimus	Sigma-Aldrich	Cat# 07741-10MG-F
Exemestane	Sigma-Aldrich	Cat# PZ0006-5MG
Floxuridine	Sigma-Aldrich	Cat# F0503-100MG
Fludarabine	Sigma-Aldrich	Cat# Y0001536-1EA
Fluorouracil	Sigma-Aldrich	Cat# F6627-5G
Fulvestrant	Sigma-Aldrich	Cat# Y0001399-1EA
Gefitinib	Sigma-Aldrich	Cat# M72803-100ML
Gemcitabine HCl	Sigma-Aldrich	Cat# G6423-10MG
Hydroxyurea	Sigma-Aldrich	Cat# H8627-5G
Ifosfamide	Sigma-Aldrich	Cat# I0060000-1EA
Letrozole	Sigma-Aldrich	Cat# Y0000685-1EA
Megestrol acetate	Sigma-Aldrich	Cat# M0513-1G
Melphalan	Sigma-Aldrich	Cat# Y0001457-1EA
Mercaptopurine	Sigma-Aldrich	Cat# 852678-1G-A
Methotrexate	Sigma-Aldrich	Cat# M1000000-1EA
Methoxsalen	Sigma-Aldrich	Cat# M3501-1G
Mitomycin C	Sigma-Aldrich	Cat# M4287-2MG
Mitotane	Sigma-Aldrich	Cat# 25925-1G-F
Mitoxantrone	Sigma-Aldrich	Cat# M6545-10MG
Oxaliplatin	Sigma-Aldrich	Cat# Y0000271-1EA
Paclitaxel	Sigma-Aldrich	Cat# T7191-5MG
Pentostatin	Sigma-Aldrich	Cat# SML0508-5MG
Plicamycin	Sigma-Aldrich	Cat# M6891-1MG
Procarbazine	Sigma-Aldrich	Cat# SML0036-10MG
Raloxifene HCl	Sigma-Aldrich	Cat# Y0001134-1EA
Rapamycin	Sigma-Aldrich	Cat# R8781-200uL
Streptozocin	Sigma-Aldrich	Cat# S0130-50MG
Sunitinib	Sigma-Aldrich	Cat# PZ0012-5MG
Tamoxifen citrate	Sigma-Aldrich	Cat# T0014000-1EA
Temozolomide	Sigma-Aldrich	Cat# 76899-10MG
Teniposide	Sigma-Aldrich	Cat# SML0609-10MG
Thalidomide	Sigma-Aldrich	Cat# T144-100MG
Thioguanine	Sigma-Aldrich	Cat# A4882-500MG
Thiotepa	Sigma-Aldrich	Cat# T6069-1G
Tretinoin	Sigma-Aldrich	Cat# PHR1187-3X100MG
Uracil mustard	Sigma-Aldrich	Cat# S375063-250MG
Vinblastine sulfate	Sigma-Aldrich	Cat# V1377-10MG
Vincristine sulfate	Sigma-Aldrich	Cat# V0400000-1EA
Vinorelbine tartrate	Sigma-Aldrich	Cat# Y0000463-1EA
Vorinostat	Sigma-Aldrich	Cat# SML0061-5MG
Zolendronic acid	Sigma-Aldrich	Cat# SML0223-10MG

(*Continued on next page*)

Continued

REAGENT or RESOURCE	SOURCE	IDENTIFIER
Critical Commercial Assays		
ENLITEN® ATP Assay System Bioluminescence Detection Kit	Promega	Cat# FF2000
RNeasy Plus Micro Kit	QIAGEN	Cat# 74034
In Situ Cell Death Detection Kit	Sigma	Cat# 11684809910
Nuclear Extraction Kit	Abcam	Cat# ab113474
Mitochondrial isolation Kit	Thermo Scientific	Cat# 89874
Deposited Data		
GEO validated RNA Sequence data accession	This paper	ID: GSE108406
Original blots used	https://data.mendeley.com/datasets/s6vkyjcpgv/draft?a=0e8f7a01-1627-41fc-b2a5-f92422529125	N/A
Experimental Models: Cell Lines		
H460 cells	ATCC	Cat# HTB-177
HCT116 cells	ATCC	Cat# CCL-247
HCT116 *TP53*$^{-/-}$ cells	Kindly donated by Dr. Vogelstein	N/A
HCT116 BAX$^{-/-}$/BAK1$^{-/-}$ cells	Generated in the lab	N/A
HCT116 *AIFM1*$^{-/-}$ cells	Generated in the lab	N/A
H4 cells	ATCC	Cat# HTB-148
HT-29 cells	ATCC	Cat# HTB-38
MCF7 cells	ATCC	Cat# HTB-2
MCF10A cells	ATCC	Cat# CRL-10317
16HBE cells	Kindly donated by Dr. DC Gruenert	N/A
Human Adipocyte Primary Cells	Celprogen (Clinisciences)	Cat# 36065-01
U-2 OS cells	ATCC	Cat# HTB-96
Experimental Models: Organisms/Strains		
Athymic Nude-*Foxn1*^{nu} female mice	ENVIGO-Harlan	Cat# 6904F
Oligonucleotides		
IDH1	Dharmacon	J-008294-11-005; J-008294-12-005
MDM2	QIAGEN	SI00300846; SI02652979
PARP1	Dharmacon	J-006656-06-0002; J-006656-07-0002
APEX1	QIAGEN	SI02663353; SI02663346
SIRT1	Sigma	Hs01_00153666; Hs01_00153667
MDM2 (TaqMan assay)	Thermo Scientific	Hs01066930_m1
Human GAPD (GAPDH) Endogenous Control	Thermo Scientific	4333764
Recombinant DNA		
pCMV-myc3-HDM2	Addgene	Cat# 20935
Software and Algorithms		
Adobe Illustrator		N/A
Microsoft Office	Microsoft	Ver 2011
GraphPrism		N/A
Image J		N/A
R software	http://www.r-project.org/	N/A
Image Lab 5.2 Software	Bio-Rad	Ver 5.2
Metamorph	Universal Imaging Corp	Ver 6.2r4
StepOnePlus Real-Time PCR System	Applied Biosystems	StepOnePlus Real-Time PCR System
Metaexpress		N/A

(*Continued on next page*)

Continued

REAGENT or RESOURCE	SOURCE	IDENTIFIER
Other		
RNAimax	Thermo Fisher Scientific	Cat# 13778075
FuGENE® HD Transfection Reagent	Promega	Cat# E2311

CONTACT FOR REAGENT AND RESOURCE SHARING

Further information and requests for resources and reagents should be directed to and will be fulfilled by the Lead Contact, Guido Kroemer (kroemer@orange.fr).

EXPERIMENTAL MODEL AND SUBJECT DETAILS

Mammalian cell lines

H460 cells were maintained at 37°C under 5% CO_2, in RPMI 1640 GlutaMax medium supplemented with 10% fetal bovine serum (FBS), 10 mM HEPES buffer, 100 units/mL penicillin G sodium and 100 μg/mL streptomycin sulfate. Human colorectal carcinoma HCT116 (WT, *BAX/BAK1*$^{-/-}$ and *AIFM1*$^{-/-}$) and HT-29, neuroglioma H4 cells and bone osteosarcoma U-2 OS cells were maintained in McCoy's 5A medium supplemented with 10% FBS, 10 mM HEPES buffer, 100 units/mL penicillin G sodium and 100 μg/mL streptomycin sulfate. Human breast cancer MCF7 cells were maintained in EMEM medium supplemented with 10% FBS, 10 mM HEPES buffer, 100 units/mL penicillin G sodium and 100 μg/mL streptomycin sulfate. Human breast non-tumorigenic MCF10A cells were maintained in DMEM/F-12 supplemented with 5% horse serum, 100 ng/mL cholera toxin, 20 ng/mL human epidermal growth factor, 10 μg/mL insulin, 0.5 μg/mL hydrocortisone, 2 mM L-glutamine and 100 units/mL penicillin G sodium and 100 μg/mL streptomycin sulfate. Human bronchial epithelial 16HBE cells were maintained in DMEM medium supplemented with 10% FBS, 10 mM HEPES buffer, 100 units/mL penicillin G sodium and 100 μg/mL streptomycin sulfate. Primary human adipocytes were purchased by Celprogen (#36065-01) and maintained in Human Adipocyte Primary Cell Culture Media (#M36065-01) with 10% FBS, 10 mM HEPES buffer, 100 units/mL penicillin G sodium and 100 μg/mL streptomycin sulfate.

Mouse model

Athymic nude female mice were maintained in specific pathogen-free conditions in a temperature-controlled environment with 12 h light, 12 h dark cycles and received food and water *ad libitum* at the animal facility of the "Centre de Recherche de Cordeliers" Paris, France. Animal experiments followed the Federation of European Laboratory Animal Science Association (FELASA) guidelines, were in compliance with EU Directive 63/2010 and were approved by the local Ethical Committee (#5271-2016042210493609v2). Athymic nude mice (7-8 week old) were obtained from ENVIGO-Harlan (Gannat, France).

METHODS DETAILS

BAY 87-2243

1-Cyclopropyl-4-(4-[(5-methyl-3-{3-[4-(trifluoromethoxy) phenyl]-1,2,4-oxadiazol-5-yl)-1H-pyrazol-1-yl)methyl]pyridin- 2-yl) piperazine (BAY 87-2243, B87, Bayer Pharma AG, Berlin, Germany) was synthesized according to the processes described in the International Patent Application Publication Number WO 2010/ 054763. For *in vitro* studies, B87 was prepared as a 10 mmol/L stock solution in dimethyl sulfoxide (DMSO) and diluted in the relevant assay media. For *in vivo* studies, B87 was administrated by daily gavage, dissolved in a 1% (v/v) solution of ethanol/solutol/water (10/40/50% respectively).

RNA interference

Cells at 60% confluence were transfected with UNR (unrelated sequence) (Sigma), IDH1 (ON-TARGET plus, Dharmacon), MDM2 (QIAGEN), PARP1 (Dharmacon), APEX1 (Ambion and QIAGEN) and SIRT1 (Sigma). siRNAs, were transfected by means of Lipofectamine RNAi max (Invitrogen) following the manufacturer instructions.

Plasmid transfection

MDM2 encoding plasmid pCMV-myc3-HDM2 was a gift from Yue Xiong (Addgene plasmid #20935). Cells were transfected by means of FuGENE® HD Transfection Reagent (Promega) following the manufacturer instructions.

Oxygen consumption

Oxygen consumption measurements (OCR) were performed using the Seahorse XFe96 Flux Analyzer and the XF cell Mito stress kit (SeaHorse Agilent, Santa Clara, CA, USA) as previously described {Sica, 2017 #40}. Briefly, 96-well plates were seeded with 12,500 H460 cells/well or 18,000 HCT116 cells/well and incubated at 37°C. After 24 h, cells were treated for 6 h with DMKG (5 mM), B87

(1 μM) or DMKG plus B87 alone or in association with RITA (50 μM) or nutlin3 (30 μM). Then incubated with 200 μL/well of Seahorse XF assay medium (102365-100) (pH 7.4) containing 2 mM glutaMAX, supplemented with 10 mM glucose and 1 mM sodium pyruvate for 1 h at 37°C without CO_2. The sensor cartridge is then loaded with oligomycin A (27 μM), carbonyl cyanide m-chlorophenyl hydrazine (CCCP, 3 μM) and rotenone (13.75 μM) to allow the Seahorse analyzer to inject them sequentially while measuring the OCR.

Glycolytic flux

Extracellular acidification rate (ECAR) measurements were performed using the Seahorse XFe96 Flux Analyzer and the XF cell Glycolysis kit (SeaHorse Agilent, Santa Clara, CA, USA) as previously described (Sica et al., 2017). Briefly, 96-well plates were seeded with 12,500 H460 cells/well or 18,000 HCT116 cells/well and incubated at 37°C. After 24 h, cells were treated for 6 h with DMKG (5 mM), B87 (1 μM) or DMKG plus B87 alone or in association with RITA (50 μM) or nutlin3 (30 μM). Then incubated with 200 μL/well of Seahorse XF assay medium (102365-100) (pH 7.4) for 1 h at 37°C without CO_2. The sensor cartridge is then loaded with glucose (90 mM), oligomycin A (30 μM) and 2DG (200 mM) to allow the Seahorse analyzer to inject them sequentially while measuring the ECAR.

Real time video

Plates were imaged using an ImageXpress Micro XL automated microscope (Molecular Devices, Sunnyvale, CA, USA) equipped with environmental control (maintaining a humidified atmosphere containing 5% CO_2 and a temperature of 37°C). Every hour during 30 h, four view fields per well were imaged at 20X magnification in the Transmitted Light (TL) and GFP channels. Acquired images were then analyzed and processed using the MetaXpress® analysis software. For each image, cells were segmented using both cell intensity in GFP channel and refringence in TL channel. Generated data were processed and statistically evaluated using the R software (https://www.r-project.org/).

Cytofluorometric assessment of apoptosis and cell cycle distribution

For apoptosis determinations, cells, after the indicated treatments, were collected and co-stained, for 30 min at 37°C, with 1 μg/mL of propidium iodide (PI) (Sigma-Aldrich), which identifies cells with ruptured plasma membranes, and either 20 nM $DiOC_6(3)$ (Molecular Probes®-Life Technologies), for the cytofluorimetric detection of dying ($DiOC_6(3)^{low}$ PI^-) and dead (PI^+) cells as previously described (Sica et al., 2016). For the assessment of cell cycle distribution, cells were plated in 12-well plates (6000 cell/well) and the cell cycle synchronized at the G_1/S border by adding thymidine (2 mM) to the medium during two consecutive nights before the indicated treatments. After the treatments the cells were collected and stained with 10 μM Hoechst 33342 in 500 μL of complete medium for 30 min at 37°C. Cytofluorometric acquisitions were performed on an Attune Ntx Flow Cytometer (ThermoFisher Scientific).

Transmission electron microscopy

For ultrastructural studies, H460 cells were fixed in 1.6% glutaraldehyde (v/v in 0.1 M phosphate buffer) for 1 h, collected by scraping, centrifuged and the pellet was post-fixed in 1% osmium tetroxide (w/v in 0.1 M phosphate buffer). Following dehydration through a graded ethanol series, cells were embedded in Epon 812 and ultrathin sections were stained with standard uranyl acetate and lead citrate. Images were taken using a Tecnai 12 electron microscope (FEI, Eindhoven, the Netherlands).

Immunofluorescence

Eight × 10^3 H460 cells were seeded into black 96-well μclear imaging plates (Greiner Bio-One) and allowed to adapt for 24 h. Thereafter, the cells were treated for 6 h before fixation in 3.7% (w/v) paraformaldehyde in phosphate buffered saline (PBS) supplemented with 1 μM Hoechst 33342 over night at 4°C. Upon fixation cells were permeabilized with 0.1% Triton in PBS for 10 min at room temperature (RT). Unspecific binding was blocked with 2% bovine serum albumin (BSA) in PBS for 10 min at RT followed by primary antibody against TOMM20 (sc-11415, Santa Cruz Biotech) or MDM2 (SMP14, Santa Cruz Biotech) diluted in BSA 2% following the manufactures recommendations overnight on shaker at 4°C. The cells were rinsed twice and stained with AlexaFluor-coupled secondary antibodies and Alexa Fluor® 594 Phalloidin (A12381 Thermo Fisher Scientific) for 1 h at RT, rinsed twice and subjected to imaging using ZEISS microscope (Axio Observer Z1 with ApoTome.2).

Sample preparation for metabolomics analysis

Cells were cultured in 6-well plates being at an approximate 80% of confluence the day of the experiment. After the corresponding treatment, wells plates are placed upon ice under chemical hood and processed as follows: wells are softly and quickly (< 2 s) rinsed with cold milliQ water (+4°C), 500 μL of cold methanol/water (9/1 v:v, −20°C, with internal standards) is added and finally scrapped for 30 s. Two wells from the same treatment were pooled in microcentrifuge tubes before adding cold chloroform (100 μL, −20°C). Solution is vortexed for 30 s and centrifuged at 15,000 rpm for 10 min at 4°C. The supernatant is collected and evaporated in microcentrifuge tubes at 40°C in a pneumatically assisted concentrator (DB3, Techne, Staffordshire, UK). Three hundred μL of methanol were added on dried extract and split in two parts of 150 μL: the first one used for the GC-MS experiment, the second one used for the LC-MS experimentation.

Untargeted metabolomics analysis of intracellular metabolites by UHPLC coupled to a quadrupole-time of flight (QTOF) mass spectrometer

Profiling of intracellular metabolites was performed on a RRLC 1260 system (Agilent Technologies, Waldbronn, Germany) coupled to a QTOF 6520 (Agilent Technologies) equipped with an electrospray source operating in full scan mode, from 50 to 1000 Da for both positive and negative ionization modes. The gas temperature was set at 350°C with a gas flow of 12 L/min. The capillary voltage was set at 3.5 kV, and the fragmentor at 120 V. Two reference masses were used to maintain the mass accuracy during analysis: *m/z*121.050873 and *m/z* 922.009798 in positive mode and *m/z* 112.985587 and *m/z* 980.016375 in negative mode. 10 μL of sample were injected on a SB-Aq column (100 mm × 2.1 mm, particle size 1.8 μm) from Agilent Technologies, protected by a guard column XDB-C18 (5 mm × 2.1 mm, particle size 1.8 μm) and heated at 40°C. The gradient mobile phase consisted of water with 0.2% of acetic acid (A) and acetonitrile (B). The flow rate was set at 0.3 mL/min. The initial condition was 98% phase A and 2% phase B. Molecules were then eluted using a gradient from 2% to 95% phase B in 7 min. The column was washed using 95% mobile phase B for 3 min and equilibrated using 2% mobile phase B for 3 min. The autosampler was kept at 4°C. Biological samples are randomized alongside 6 to 7 quality control samples that were assembled by pooling all experimental samples and that were injected at regular intervals.

Targeted analysis of intracellular metabolites by UHPLC coupled to a Triple Quadrupole (QQQ) mass spectrometer

Targeted analysis was performed on a RRLC 1260 system coupled to a Triple Quadrupole 6410 (Agilent Technologies) equipped with an electrospray source operating in positive mode. The gas temperature was set at 350°C with a gas flow of 12 L/min. The capillary voltage was set at 3.5 kV. Ten μL of sample were injected on a Column Zorbax Eclipse XDB-C18 (100 mm x 2.1 mm, particle size 1.8 μm) from Agilent technologies, protected by a guard column XDB-C18 (5 mm × 2.1 mm, particle size 1.8 μm) and heated at 40°C. The gradient mobile phase consisted of water with 2 mM of DBAA (A) and acetonitrile (B). The flow rate was set at 0.2 mL/min, and the gradient as follows: initial condition of 90% phase A and 10% phase B is maintained for 4 min and then from 10% to 95% phase B over 3 min. The column was washed using 95% mobile phase B for 3 min and equilibrated using 10% mobile phase B for 3 min. The autosampler was kept at 4°C. Biological samples were randomized alongside 6 to 7 QC samples.

Fluxomic analysis

Glucose-D U-^{13}C6 (CLM-1396, Eurisotop) was used to measure glucose uptake and flux *in vitro*. The samples extraction protocol is the same described above with the difference that the extraction solvent did not contain any labeled internal standards. Derivatization of GC aliquot was handle in glass tubes. Fifty μL of O-ethylhydroxylamine hydrochloride (20 mg/mL in pyridine; Sigma-Aldrich, Saint Louis, MO, US) was added to the dried extracts, stored at room temperature in the dark for 16 h. Silylation was carried out with 80 μL of N-tert-butyldimethylsilyl-N-methyltrifluoroacetamid (Sigma-Aldrich) at 40°C for 60 min. The GC-MS/MS method was performed on a 7890A gas chromatography (Agilent Technologies) coupled to a triple quadrupole 7000C (Agilent Technologies) equipped with an electronic impact source (EI) operating in positive mode. The front inlet temperature was 250°C, the injection was performed in splitless mode. The transfer line and the ion-source temperature were 250°C and 230°C, respectively. The septum purge flow was fixed at 3 mL/min, the purge flow to split vent operated at 80 mL/min during 1min and gas saver mode was set to 15 mL/min after 5 min. The helium gas flowed through the column (J&W Scientific HP-5MS, 30 m x 0.25 mm, i.d. 0.25 mm, d.f.; Agilent Technologies) at 1 mL/min. Column temperature was held at 70°C for 1 min, then raised to 120°C (15°C/min), followed by a step of 1 min at this temperature, and a second step to reach 325°C (10°C/min), holding this temperature for 3 min. The collision gas was nitrogen. The scan mode used is the MRM for biological samples with the Q1 corresponding to the maximally derivatised molecule and with Q3 corresponding to a typical fragment of silyl group (73 or 147). Peak detection and integration of the isotopomers of 37 analytes were performed using the Agilent Mass Hunter quantitative software (B.07.01). After manual verification and QC protocols, 31 isotopomer distributions entered data analysis and interpretation and manually checked. All chemicals were purchased from Sigma-Aldrich. The experiments, with 4-5 replicates per condition, were repeated three times.

Intracellular ATP assessment

ENLITEN® ATP Assay System Bioluminescence Detection Kit for ATP Measurement, purchased by Promega, has been used to assess the intracellular content of ATP as described in the manufacturing protocol.

Immunoblotting

Cells were seeded, treated and washed with cold PBS and lysed in a buffer containing 1% Nonidet P-40, 20 mM HEPES (pH 7.9), 10 mM KCl, 1 mM EDTA (Ethylenediaminetetraacetic acid), 10% glycerol plus cOmplete, Mini, EDTA-free Protease Inhibitor Cocktail (11836170001, Sigma-Aldrich) and phosphates inhibitor (PhosSTOP, Sigma Aldrich). Lysates were separated (20 μg proteins per lane) on pre-cast 4%–12% polyacrylamide NuPAGE Novex Bis-Tris gels (Invitrogen-Life TechnologiesTM) to ImmobilonTM membranes (Millipore Corporation, Billerica, MA, USA). Membranes were incubated in 0.1% Tween- 20 (v:v in Tris-buffered saline (TBS)) supplemented with 5% non-fat powdered milk (w:v in TBS) for 1 h to saturate unspecific binding sites and sliced in parts to allow for the simultaneous detection of proteins with different molecular weight in the same experiment. Thereafter, membranes were incubated overnight at 4°C with primary antibodies specifics and were detected with appropriate horseradish peroxidase (HRP)-labeled secondary antibodies (Southern Biotech, Birmingham, AL USA) and the SuperSignal West Pico chemiluminescent

substrate (Thermo Fischer Scientific, Waltham, MA, USA). Chemiluminiscence images were acquired on an ImageQuant LAS 4000 digital imaging system (GE Healthcare Life Sciences, Pittsburgh, PA, USA).

Carboxyfluorescein succinimidyl ester (CFSE) staining

CellTrace™ CFSE dye labeling was conducted as previously described (Vitale et al., 2013). Briefly, the cells (1×10^6 cells/mL) were detached and incubated in PBS containing CellTrace™ CFSE (#C34554, Thermo Fisher) (5 μM) for 10 minutes and then plated the day before the treatments. The fluorescein-derived intracellular fluorescent label is divided equally between daughter cells upon cell division. After the treatment cell were collected and analyzed by cytofluorimeter for the detection of CFSE intensity.

In vivo experiments

For tumor growth experiments, $5x10^6$ H460 or HCT116 cells were inoculated subcutaneously (near the thigh) into the mice, and tumor surface (longest dimension x perpendicular dimension) was routinely monitored using a common caliper. When the tumor surface reached 25–35 mm^2, mice were treated either with B87 (1 mg/kg) or vehicle control consisting in a solution of ethanol/Solutol® HS 15/water (10/40/50%), once daily by oral gavage, alone or in combination with DMKG (100 mg/kg, diluted in PBS) or PBS, administered intratumorally once every two days.

For *in situ* cell death detection, paraffin sections were processed with proteinase K. All slides were assessed by TUNEL positive cells using *In Situ* Cell Death Detection Kit, purchased from Sigma-Aldrich (St. Louis, MO, USA). Staining was visualized by using the permanent red kit (Dako). Each slide was examined using a Zeiss Axiophot microscope. A single representative whole tumor tissue section from each animal was digitized using a slide scanner. Prior to computer analysis, regions of interest were drawn to exclusively select tumor tissue and to eliminate both nontumor tissue and large stained artifact deposits, if any.

Dead cells labed by TUNEL method are identified by the ManualROI_Nuclei (Positive versus Negative) algorithm in Definiens Tissue Studio (Definiens AG, Munich, Germany). Briefly, nuclei stained with TUNEL method were automatically detected according to their IHC staining spectral properties in manually selected Regions Of Interest (exclusion of areas of necrosis, preparation artifacts ...). Results are expressed as a number of stained cells per mm^2 of analyzed tissue. All *in vivo* experiments were randomized and blinded, and sample sizes were calculated to detect a statistically significant effect.

Gene expression analysis

Total RNA from cell lines was purified using RNeasy Mini Kit (QIAGEN), followed by column purification with RNeasy Mini Kit (QIAGEN). Following the manufacturer's instructions, Superscript III Reverse Transcriptase (Invitrogen) was used with random hexamers (Promega) for generation of cDNA. Quantitative PCR was performed on a StepOnePlus Real-Time PCR System (Applied Biosystems) using TaqMan Gene Expression Master Mix (Applied Biosystems) and the following TaqMan Gene Expression Assays: human MDM2 (Hs01066930_m1) and human GAPDH (4333764) purchased by ThermoFisher Scientific.

RNA-sequencing

The libraries were prepared following the Tru-seq mRNA protocol from Illumina, starting from 1 ug of high quality total RNA. Paired end (2 × 75) sequencing was performed on an Illumina Nextseq 500 platform. The RNA concentration was measured using a fluorometric Qubit RNA HS assay (Life Technologies, Grand Island, New York, USA). The quality of the RNA (RNA integrity number 8.2) was determined on the Agilent 2100 Bioanalyzer (Agilent Technologies, Palo Alto, CA, USA). To construct libraries, 1 μg of high quality total RNA sample (RIN > 8) was processed using Truseq stranded mRNA kit (Illumina) according to manufacturer instructions. Briefly, after purification of poly-A containing mRNA molecules, mRNA molecules are fragmented and reverse-transcribed using random primers. Replacement of dTTP by dUTP during the second strand synthesis will permit to achieve the strand specificity. Addition of a single A base to the cDNA is followed by ligation of adapters. Libraries were quantified by qPCR using the KAPA Library Quantification Kit for Illumina Libraries (KapaBiosystems, Wilmington, MA) and library profiles were assessed using the DNA High Sensitivity LabChip kit on an Agilent Bioanalyzer. Libraries were sequenced on an Illumina Nextseq 500 instrument using 75 base-lengths read V2 chemistry in a paired-end mode. After sequencing, a primary analysis based on AOZAN software (ENS, Paris) was applied to demultiplexe and controls the quality of the raw data (based of FastQC modules / version 0.11.5). Obtained fastq files were then aligned using Star algorithm (version 2.5.2b) and quality control of the alignment realized with Picard tools (version 2.8.1). Reads were then count using Feature count (version Rsubread 1.24.1) and the statistical analyses on the read counts were performed with the DESeq2 package version 1.14.1 to determine the proportion of differentially expressed genes between two samples.

RNA-seq data analysis

RNA-Seq data analysis was performed by GenoSplice technology (www.genosplice.com). Sequencing, data quality, reads repartition (e.g., for potential ribosomal contamination), and insert size estimation were performed using FastQC, Picard-Tools, Samtools and rseqc. Reads were mapped using STARv2.4.0 (Dobin et al., 2013) on the hg19 Human genome assembly. Gene expression regulation study was performed as already described (Noli et al., 2015). Briefly, for each gene present in the Human FAST DB v2016_1 annotations, reads aligning on constitutive regions (that are not prone to alternative splicing) were counted. Based on these read counts, normalization and differential gene expression were performed using DESeq2 (Love et al., 2014) on R (v.3.2.5). Only genes expressed in at least one of the two compared experimental conditions were further analyzed. Genes were considered as

expressed if their rpkm value was greater than 98% of the background rpkm value based on intergenic regions. Results were considered statistically significant for uncorrected p values $\leq$ 0.05 and fold-changes $\geq$ 1.5.

Unsupervised analysis

Clusterings and heatmaps have been performed using ''dist'' and ''hclust'' functions in R, using Euclidean distance and Ward agglomeration method.

Pathway/Gene Ontology (GO) analysis and transcription factor analysis

Analysis for enriched GO terms, KEGG pathways and REACTOME pathways were performed using DAVID Functional annotation Tool (v6.8). GO terms and pathways were considered as enriched if fold enrichment $\geq$ 2.0, uncorrected *p-value* $\leq$ 0.05 and minimum number of regulated genes in pathway/term $\geq$ 2.0. Analysis was performed three times: using all regulated genes, using upregulated genes and using downregulated genes only. Union of these three analyses was made to provide a single list of results. Analysis for transcription factor was performed using orthologous genes between mouse and human and DAVID Functional annotation Tool (v6.8). Orthologous genes are aggregated in FAST DB from Ensembl compara. The same thresholds and methods were used as GO terms and Pathway analysis but with human data.

Monitoring mitochondrial pyruvate carrier activity

RESPYR (for REporter Sensitive to PYRuvate) biosensor measures bioluminescence resonance energy transfer (BRET) between the two subunits of the MPC, MPC2 fused to the donor group RLuc8 (a variant of Renilla luciferase) and MPC1 fused to the acceptor group Venus (a variant of yellow fluorescent protein). In this system, addition of the luciferase substrate coelenterazine H only yields a signal corresponding to the fluorescence emission spectrum of Venus when the two subunits physically approach each other during the transport of pyruvate (Compan et al., 2015).

QUANTIFICATION AND STATISTICAL ANALYSIS

Data were analyzed with Microsoft Excel (Microsoft Co., Redmont, WA, USA) and Prism 6.0 (GraphPad, San Diego, CA, USA). Data are presented as means ± SD or SEM. The figure legends describe the statistical tests used and value of *n* for each experimental group.. All cytometric quantifications of cell death were performed by Student t test calculated between the sum of ($DiOC_6(3)^{low}$ PI^-) and (PI^+) cells. *P*-values were computed by unpaired Student's t tests or two-ways ANOVA followed by Sidak's multiple comparisons test. Comparisons of Kaplan–Meier survival curves were performed using the log-rank Mantel–Cox test. All reported tests are two-tailed and were considered significant at *p-value*s < 0.05 (*p < 0.05, **p < 0.01, ***p < 0.001).

DATA AND SOFTWARE AVAILABILITY

The accession number for the RNA-seq data reported in this paper is: GSE108406.

The original blots used in this paper are reported in: Mendeley datashet